Parametric Study and Multi-Objective Optimization of Fixed-Bed Fischer–Tropsch Reactor

Moazami, Nima; Wyszynski, Miroslaw; Rahbar, Kiyarash; Tsolakis, Athanasios

DOI:
10.1021/acs.iecr.7b02025

Document Version
Peer reviewed version

Citation for published version (Harvard):
Moazami, N, Wyszynski, M, Rahbar, K & Tsolakis, A 2017, 'Parametric Study and Multi-Objective Optimization of Fixed-Bed Fischer–Tropsch Reactor: The Improvement of FT Synthesis Products Formation and Synthetic Conversion', Industrial & Engineering Chemistry Research, vol. 56, no. 34, pp. 9446–9466. https://doi.org/10.1021/acs.iecr.7b02025

Parametric Study and Multi-Objective Optimization of Fixed-Bed Fischer–Tropsch Reactor: The Improvement of FT Synthesis Products Formation and Synthetic Conversion

Nima Moazami*, Miroslaw Lech Wyszynski, Kiyarash Rahbar, Athanasios Tsolakis

Department of Mechanical Engineering, College of Engineering and Physical Sciences, The University of Birmingham, Edgbaston, Birmingham, B15 2TT, UK

*Corresponding author's email address: nxm958@alumni.bham.ac.uk

Abstract:

A mathematical model of a fixed-bed reactor for Fischer–Tropsch Synthesis (FTS) over 37% Co/SiO_2 catalyst was developed to investigate the performance of the whole process for products' selectivity and syngas conversion. The model was capable of calculating the changes of reactant and products' concentrations, partial pressures, conversion and selectivity. In the previous study, a series of combined novel FT and water gas shift (WGS) reaction mechanisms (eight elementary FT reaction pathways along with seven WGS kinetics models) were developed in order to calibrate and validate the mathematical model along with reaction kinetics at different experimental conditions. Such mathematical model with reaction networks can be used as a key tool to emphasise the most significant facts of FTS catalysis and chemistry. Integration of the Global Search optimization algorithm with the developed model was explained for estimation of kinetics parameters. Data analyses were carried out to assure that the predicted model results as well as kinetic parameters are significantly relevant and physically meaningful. Parametric studies were performed to numerically investigate the effects of operating conditions (e.g. reaction temperature, total pressure, space velocity and H_2/CO molar ratio) on products' selectivity and reactant conversion. These parameters were then included in a multi-objective optimization in MATLAB using NSGA–II to optimize the CO_2 and HC products' selectivity and syngas conversion. The optimization process gives rise to a set of trade-off optimal solutions (Pareto-optimal solutions) which is used as a dynamic database depending on the specific requirement. A different operating condition can be selected from such database which privileges the optimization of a particular output (e.g. conversion and selectivity).

Keywords: Fischer–Tropsch Synthesis; Fixed-Bed Reactor; Mathematical Modelling; Multi-Objective Optimization; Liquid Fuel Production; Biofuels Tecchnology

1. Introduction

Nowadays there is a worldwide demand to develop energy-efficient and economical processes for sustainable production of alternative chemical compounds and fuels as a substitute for those emerging from petroleum. The excessive dependency of the world on conventional fossil fuels risks the future of the globe. The consistent existence of the present condition will result in an increase of the average temperature of ocean surfaces and global land by 5℃ in 2100; this will cause rising sea levels, which will be the next global crisis [1]. Climate

change and global warming, due to the increase of carbon dioxide (CO_2) concentration in the atmosphere formed from the combustion of fossil fuel, and also air pollution, are major environmental concerns as a consequence of their direct influence on human breath and life. As a result, environmental agencies everywhere in the world have delivered more severe regulations to meet the current and forthcoming threats caused by emissions to the atmosphere e.g. the control of emission standards for particulates from diesel vehicles and residual sulphur in diesel fuel. All these facts have lately increased a renewed interest in Fischer–Tropsch Synthesis (FTS). FTS can be defined as the means of indirect liquefaction, in which synthesis gas (a mixture of predominantly CO and H_2) obtained from either coal, peat, biomass or natural gas is catalytically converted to a multicomponent mixture of gaseous, liquid and solid hydrocarbons [2]. The increased interest in FTS is due to its ability to produce ultra-clean diesel oil fraction with a high cetane number (typically above 70) without any aromatic, sulphur and nitrogen compounds; with a very low particulate formation; and CO emissions [3-6]. Liquid fuels produced from biomass via FTS have great potential to produce high-performance, environmentally friendly clean and high-quality transportation fuels; mainly due to the absence of aromatic compounds, SO_x (sulphur oxides) and NO_x (nitrogen oxides). Generally, modern FTS is conducted over the liquid phase slurry reactor, the gas phase fluidized bed reactor or the gas phase fixed-bed reactor [7]. The fixed-bed reactor has several advantages such as the absence of the requirement to separate the catalyst from the product, the ease of the scaling up from a single tube to a pilot plant and shutdown robustness compared with slurry bed reactor [8-9]. Shell and Sasol are the pioneers and world leading companies for large scale FT liquids production using fixed-bed reactor and slurry bed reactor, respectively. It has been found that the VIII group metals such as nickel, cobalt, ruthenium and iron can be activated as a catalyst for FT reaction [10]. However, only iron and cobalt-based catalysts appear to be feasible and suitable on an industrial scale economically [10-11]. Among different solid catalysts, cobalt is considered the most favourable catalyst for the production of long-chain hydrocarbons due to its high selectivity to linear paraffins, high activity, and high resistance to deactivation [12-13].

The kinetics description and mathematical modelling of FTS is crucial for the process design, simulation, optimization, and it is quite challenging due to the complexity of the reaction pathway and products involved in this process. Currently, there are three main aspects for consideration regarding the FTS processes. Firstly, there exists the FTS reaction mechanism, the details of which are still not fully understood. Very recently, Moazami *et al.* [14] developed a comprehensive detailed kinetics of FT and water gas shift (WGS) reaction for cobalt-based FTS process conducted in a fixed-bed reactor. Furthermore, from the outlook of chemical engineering, there is the design and scale-up of the commercial FTS plant in which studies of the mathematical model, parametric analyses as well as numerical optimization play significant roles. An optimal design of a commercial-scale reactor requires detailed information of the hydrodynamics and the reaction kinetics, as well as the mathematical model of the catalytic reactor. To achieve an optimum in performance for the whole process, the mathematical development of the kinetics and the reactor model are essential. Also, the details of the products' distribution, selectivity and reactants conversion should be achieved by the developed mathematical model [15]. By modelling and optimizing the reactor's operation, it is possible in many cases to achieve significantly enhanced throughput; better and more consistent product quality; rising conversion and selectivity; as well as a significant effect on the scaling up of the processes from the laboratory to production scale. Only a few studies [16-25] are available on the

basis of the development of a mathematical model of a fixed-bed reactor for FTS. Typically, the plug flow reactor model is approximated in fixed-bed reactors so that the reaction components and reaction conditions of the medium vary continuously along the axial length of the catalytic bed. The driving force for synthesis is maximized and, in the absence of heat and mass transfer limitations, fixed-bed reactor technology is the most efficient reactor type for synthesis [26]. Compared to slurry and fluidized bed reactors, at the same level of conversion, the products from a fixed-bed reactor can be expected to have higher hydrogenation activity (i.e. less olefins and oxygenates). For instance, considering Fe-LTFT synthesis at 521 K, 8 bar and 50–60% CO conversion, the C_2-C_4 olefin to paraffin ratio for fixed-bed FTS is typically 0.09, 0.9, and 1.2 respectively; whereas for slurry bed synthesis it is typically 3.7, 5.6, and 4.5 [26-27]. Fixed-bed reactors are employed in LTFT processes for mainly diesel and waxes production [28]. The main types of catalysts used in LTFT reactors are Co-based catalysts, which have a high selectivity towards diesel and high molecular weight waxes. Fe-based catalysts can also be utilized in LTFT reactors; although, it has been reported that the operating temperature cannot exceed 533 K, as the reactor will be blocked with carbon deposition [29].

There are very limited studies published in the literature that investigated the parametric study of FTS to improve its catalytic performance and there is lack of studies in the literature that studied the numerical optimization of the process to achieve an optimal solution (e.g. selectivities and conversion). Dry [30] indicated that ‘‘for all FT catalysts an increase in operating temperature results in a shift in selectivity towards lower carbon number products and to more hydrogenated products. The degree of branching increases and the amount of secondary products formed such as ketones and aromatics also increases as the temperature is raised’’ [31]. Jager *et al.* [32] investigated the response of different kinetic rate equations to a change in operating pressure while keeping all other variables constant. The effect of operating pressure by some kinetic equations for cobalt showed the predicted increase in conversion solely due to an increase in operating pressure. Bukur *et al.* [33] investigated the effect of process conditions on olefin selectivity during conventional and supercritical FTS on iron catalyst in a fixed-bed reactor. Bai *et al.* [34] investigated the effect of temperature, total pressure, space velocity and the ratio of H_2/CO on Fe-Mn catalyst performance. It was found that the catalyst has high activity at 533 K, CO conversion increased from 89.3 to 95.6% indicating that the operation window for temperature over the Fe-Mn catalyst is very broad.

Here, a mathematical model of a fixed-bed reactor along with a detailed numerical simulation as well as a recently developed comprehensive kinetics model [14] is developed to emphasise the most significant facts of FTS catalysis. Parametric studies are conducted in order to illustrate the effects of operating conditions such as total pressure, reaction temperature, GHSV and H_2/CO molar ratio on the performance of FTS over supported Co-based catalyst with respect to productivity, selectivity and feed conversion. Multi-objective optimization process is conducted in MATLAB platform using Non-Dominated Sorting Genetic Algorithm (NSGA–II) to optimize the CO_2, paraffin and olefin hydrocarbon products’ selectivities as well as syngas conversion. The Pareto-front solutions can be used as a dynamic database depending on the specific requirement. A different operating condition can be selected from such database which privileges the optimization of a particular output (e.g. conversion and selectivities).

2. Methodology

A numerical analysis and mathematical modelling can be used as an effective tool to provide knowledge about a catalytic reaction. The whole process involved in the development of mathematical model and kinetics modelling of the FTS process can be found in supplementary material.

Focusing on the phenomena occurring in the reactor reduces the apparent diversity into a small number of models or basic reactor types. The phenomena taking place in the reactor can be broken down into transfer of mass, heat and momentum as well as chemical reactions. The chemical reaction kinetics of FTS were comprehensively investigated in the previous work [14]. The design and modelling of the reactor is on the basis of equations that describe the above-mentioned phenomena.

2.1. Model Assumptions and Equations

The FTS process was carried out in a stainless steel mini-scale fixed-bed reactor with an inner diameter of 15.7 mm and a reactor length of 52.83 cm. A mathematical model of the reactor was developed based on the following assumptions. A series of eggshell cobalt catalysts supported with silica powder were used. The detail of the catalyst and support materials was discussed in the previous work in section 2 [14]. The utilization of the eggshell catalyst in a mini-scale fixed-bed reactor is an advanced technique, which can overcome the mass transfer limitation due to diffusion limitations in catalyst pellets in the fixed-bed reactor system [1, 35]. Here, the catalyst was loaded in the reactor in powder form (2 g catalyst with particle size of 75-150 μm) in order to prevent internal mass transfer limitations. The above assumption was also taken into account by other investigators utilizing a catalyst in the form of powder to prevent the internal mass transfer limitations [36]. Based on the above justifications, the effects of the internal and external mass transfer resistances (interphase and intraparticle mass transport) were neglected; hence only the rate of surface reaction in the reactor was the controller.

In order to describe the kinetics of the experimental conditions the reactor model was assumed to be a plug-flow 1D pseudo-homogeneous state. Therefore, transportation in the catalyst's pores (transport phenomena in solid phase) was not considered, to avoid the unsolvable difficulties in the integration of the reactor model embedded in a parameter optimization procedure [37].

Also, in order to improve the temperature distribution along the catalytic beds, minimize the formation of heat spots and prevent the temperature gradients caused by the strongly exothermic FTS reaction, 2 g of the pre-calcined catalyst was weighted for each experiment and then diluted with 12 g of inert silicon carbide (mesh particle size 200-450). The dilution of the catalyst avoids local hot-spots [1]. Dilution of a solid catalyst (in powder form) with inert diluent (i.e. silicon carbide) is a common practice in the laboratory scale FTS process to have better heat removal as well as an effective use of a catalyst bed [38]. In addition, to provide a uniform wall temperature along the reactor bed length, a metal jacket was installed between the furnace and the fixed-bed reactor and it surrounded the reactor. A steady-state condition was assumed so that there was no change over time including catalytic activity, selectivity and stability. Based on the above assumptions, a 1D steady-state

pseudo-homogeneous mathematical model was developed to describe the hydrodynamic of the fixed-bed reactor for FTS. Equation 1 and 2 describe the conservation equations of i^{th} species with respect to concentration and partial pressure, respectively. The mole balance equations were first order ordinary differential equations (ODEs). For homogeneous system $\alpha^* = 1$, whereas for heterogeneous catalytic reactions α^* equals to the bulk density of the catalyst (ρ_B) which is determined by the ratio of mass of the catalyst (m_{cat}) over the packed bed reactor volume (V_l). The u_s, C_i, β, v_{ij}, R_j, NR, R_g, p_i, P_T, and ρ_f represent superficial velocity, molar concentration of species *'i'*, volume fraction of active catalyst, stoichiometric coefficient of component 'i' in reaction 'j', rate of reaction 'j', number of reactions, universal gas constant, partial pressure of species 'i', total pressure and density of the mixture respectively. Gas velocity was calculated from the continuity equation (Equation 3).

$$u_s \frac{\partial C_i}{\partial z} = \alpha^* \beta \sum_{j=1}^{NR} v_{ij} R_j - C_i \frac{\partial u_s}{\partial z} \quad \text{Equation 1}$$

$$\frac{u_s}{R_g T} \frac{\partial p_i}{\partial z} = \alpha^* \beta \sum_{j=1}^{NR} v_{ij} R_j - \left(\frac{P_T}{R_g T} \frac{\partial u_s}{\partial z} \right) \quad \text{Equation 2}$$

$$\rho_f \frac{\partial u_s}{\partial z} = -u_s \frac{\partial \rho_f}{\partial z} \quad \text{Equation 3}$$

Density of the fluid mixtures was computed by applying the chain rule to the ideal gas law (Equation 4). In this equation, the average molar weight of the fluid mixture (M_m) was simply determined by the molar mass of each species (M_i) and its mole fraction in the mixture (Y_i) (Equation 5).

$$\frac{\partial \rho_f}{\partial z} = \frac{\partial \left(\frac{P_T M_m}{R_g T} \right)}{\partial z} = \frac{M_m}{R_g} \frac{1}{T} \frac{\partial P_T}{\partial z} - \frac{M_m P_T}{T^2 R_g} \frac{\partial T}{\partial z} \quad \text{Equation 4}$$

$$M_m = \sum_{i=1}^{NS} Y_i M_i \quad \text{Equation 5}$$

The classic Ergun equation is the most popular equation used to calculate overall pressure drop through catalytic packed bed reactors. Equation 10 is the general form of this equation. The first term on the right side of this equation corresponds to the Blake-Kozeny equation for laminar flow, while the second term corresponds to the Bruke-Plummer equation for turbulent flow. The Hagen-Poiseuille equation, expressing the pressure drop for laminar flow in an empty conduit, when written in the form of (Equation 11), leads to a friction factor (f) in the form of Equation 6.

$$f = \frac{(1-\varepsilon)^2}{\varepsilon^3} \frac{36}{G d_p / \mu_m} \quad \text{Equation 6}$$

In this equation, μ_m, ε, G, d_p represent molecular viscosity of the mixture, void fraction, mass velocity and particle diameter respectively. Since the channels in a packed bed are not straight, a correlation factor of 25/6 had to be introduced by Ergun to fit the experimental data, so that (Equation 6) becomes:

$$f = \frac{(1-\varepsilon)^2}{\varepsilon^3}\frac{150}{Gd_p/\mu_m} \qquad \text{Equation 7}$$

Considering the Burke and Plummer equation for highly turbulent flow in a channel, it leads to a following form of friction factor:

$$f = 1.75\frac{1-\varepsilon}{\varepsilon^3} \qquad \text{Equation 8}$$

Adding both contributions Ergun proposed,

$$f = \frac{1-\varepsilon}{\varepsilon^3}\left[a + \frac{b(1-\varepsilon)}{Re}\right] \qquad \text{Equation 9}$$

With a=1.75 and b=150. Handley and Heggs [1968] derived a value of 1.24 for *a* and 368 for *b*. McDonald *et al.* [1979] proposed a = 1.8 for smooth particles and 4.0 for rough particles and b = 180 [39].

Consequently, the Ergun law was applied to calculate the overall pressure drop (dP_T) along the reactor bed length (L) and among different parametrization for the friction factor, Equation 12 was assumed to be the proper form of the friction factor for the flow in the fixed-bed reactor [39].

$$\frac{dP_T}{L} = \frac{150G\mu_m}{{d_p}^2\rho_f}\frac{(1-\varepsilon)^2}{\varepsilon^3} + 1.75\frac{G^2}{\rho_f d_p}\frac{(1-\varepsilon)}{\varepsilon^3} \qquad \text{Equation 10}$$

$$\frac{dP_T}{dz} = -f\frac{u_s^2\rho_f}{d_p} \qquad \text{Equation 11}$$

$$f = \frac{(1-\varepsilon)^2}{\varepsilon^3}\frac{36(25/6)\mu_m}{\rho_f u_s d_p} \qquad \text{Equation 12}$$

The model aimed at predicting the axial profiles of radially averaged concentrations, partial pressure, feed conversion and selectivity of different compositions at different operating conditions (which were available for calibration and validation), with respect to reaction temperature, total pressure and space velocity in a wide range of 503-543 *K*, 10-25 *bar* and 1.8-3.6 $L\ g_{cat}^{-1}\ h^{-1}$, respectively.

2.2. Reactor Performance Criteria

Some intensive dimensionless quantities were expressed to characterize the operation of an FT reactor and presented the methods used for reactor performance measurement and analysis. The conversion is related to the composition of the reactants and was defined for carbon monoxide and hydrogen, which by definition, its value is between 0 and 1. Therefore, Equation 13 was employed to quantify the fraction of carbon monoxide and

hydrogen that has been consumed in the FT reactor. The conversion only depends on the boundaries of the system, "in" and "out" [40]. It should be mentioned that that none of the reactions in the FTS process produce carbon monoxide and hydrogen.

$$Conversion = x_i\,(\%, i: CO, H_2) = \frac{C_{in,i} - C_{out,i}}{C_{in,i}} \times 100 \qquad \text{Equation 13}$$

Equation 14 to Equation 16 were used to measure the portion of reactant converted to desired and undesired products in the FT process. Since the carbon dioxide is the only co-product which consumed the carbonaceous reactant to be produced, Equation 14 was used to compute the selectivity of CO_2 species which is the ratio of concertation of CO_2 produced to that of CO consumed.

$$Carbon\ dioxide\ selectivity\ =$$

$$S_{CO_2}(\%) = \frac{C_{out,CO_2}}{C_{in,CO} - C_{out,CO}} \times 100 \qquad \text{Equation 14}$$

$$Lighter\ hydrocarbon\ selectivity =$$

$$S_{x\,(C_1 - C_4)}\,(\%) = \frac{C_{out,C_n}}{C_{in,CO} - C_{out,CO} - C_{out,CO_2}} \times 100 \qquad \text{Equation 15}$$

$$Total\ liquid\ selectivity =$$

$$S_{C_{5+}}(\%) = 100 - \left(S_{CO_2} + S_{HC_1} + S_{HC_2} + S_{HC_3} + S_{HC_4}\right) \qquad \text{Equation 16}$$

In Equation 16, the desired products' selectivity was determined relative to the amount of carbon monoxide reactant converted to hydrocarbon products; hence, in the denominator, the moles of carbon monoxide converted to carbon dioxide, was subtracted. The numerical values of products' selectivity are between 0 to 100% based on their definitions. The summation of all products' selectivity must be equal to 100%.

Equation 16 describes how to determine the selectivity of the heavy hydrocarbons (carbon number ≥ 5). As some of the compounds in a standard gas bottle used for quantitative analysis of gaseous products by GC-FID (gas chromatography flame ionization detector) were not available, the measurement of the quantities of particular constituents presented in the gaseous products downstream of a reactor was not possible; therefore, the product selectivity of detailed hydrocarbons was measured up to hydrocarbons with a carbon number ≤ 7.

2.3. Reaction Kinetics Modelling

In the previous work [14], a comprehensive plausible mechanism-derived FT kinetics models with eight elementary reaction pathways along with seven WGS kinetics models were developed. Such reaction networks were investigated to fit and validate against the experimental results which can be used as a key tool to emphasise the most significant facts of FTS catalysis and chemistry. The obtained results in [14] showed that the combined developed model FT–III with RDS-2 (R.4, 8-15)/WGS-VII with RDS-4 (R.4), exhibited excellent agreement with the measured data. The proposed pathway and elementary reaction steps for both FTS and WGS reaction are illustrated in Table 1.

Table 1 Sequence of elementary reaction steps of FTS reaction in the present study [14]

Model	No.	Elementary reaction steps	Model	No.	Elementary reaction steps
FT–III	1	$CO + \psi \rightleftarrows CO - \psi$	WGS-VII	1	$CO + \sigma \rightleftarrows CO - \sigma$
	2	$H_2 + 2\psi \rightleftarrows 2H - \psi$		2	$H_2O + 2\sigma \rightleftarrows H - \sigma + OH - \sigma$
	3	$CO - \psi + H - \psi \rightleftarrows HCO - \psi + \psi$		3	$CO - \sigma + OH - \sigma \rightleftarrows CHO_2 - \sigma + \sigma$
	4	$HCO - \psi + H - \psi \rightleftarrows HCOH - \psi + \psi$		4	$CHO_2 - \sigma \rightleftarrows H - \sigma + CO_2$
	5	$HCOH - \psi + \psi \rightleftarrows CH - \psi + OH - \psi$		5	$2H - \sigma \rightleftarrows H_2 + 2\sigma$
	6	$OH - \psi + H - \psi \rightleftarrows H_2O + 2\psi$			
	7	$CH - \psi + H - \psi \rightleftarrows CH_2 - \psi + \psi$			
	8	$CH_2 - \psi + H - \psi \rightarrow CH_3 - \psi + \psi$			
	9	$CH_3 - \psi + H - \psi \rightarrow CH_4 + 2\psi$			
	10	$CH_2 - \psi + CH_2 - \psi \rightarrow C_2H_4 + 2\psi$			
	11	$CH_2 - \psi + CH - \psi \rightarrow C_2H_3 - \psi + \psi$			
	12	$C_{n-1}H_{2n-1} - \psi + CH_2 - \psi \rightarrow C_nH_{2n+1} - \psi + \psi\ ;\ n \geq 2$			
	13	$C_nH_{2n+1} - \psi + H - \psi \rightarrow C_nH_{2n+2} + 2\psi$			
	14	$CH_2 - \psi + C_{n-1}H_{2n-3} - \psi \rightarrow C_nH_{2n-1} - \psi + \psi$			
	15	$C_nH_{2n-1} - \psi + H - \psi \rightarrow C_nH_{2n} + 2\psi$			

The goodness of fit was assessed by mean absolute percentage deviation (see section 3.4 of supplementary material) and statistically analysed by employing the F-statistic as explained (see section 3.5 of supplementary material). In addition, it was shown that the obtained kinetic parameters were statistically significant by using the t-statistic (see section 3.6 of supplementary material). The estimated kinetic parameters for the comprehensive kinetic model over a Co/SiO_2 catalyst are listed in Table 2 and the details of kinetic parameters' estimation were discussed in the previous work [14]. The above-mentioned reaction mechanisms for the formation of paraffins and olefins' products as well as CO_2 are illustrated in Figure 1**Error! Reference source not found.**. The kinetic equations were developed and discussed comprehensively in the previous study [14]. Herein, the FT and WGS reaction pathways along with the corresponding rate expressions are tabulated in Table 3 to Table 5.

Table 2 Optimum values of estimated kinetic parameters of comprehensive combined FT−III (RDS-2) and WGS-VII (RDS-4) [14]

Kinetic parameter	Unit	Value	t_{value}	Kinetic parameter	Unit	Value	t_{value}
$k_{0,meth}$	$mol\ kg^{-1}\ s^{-1}$	5.10×10^7	162.84	$k_{0,4}$	$mol\ kg^{-1}\ s^{-1}$	9.25×10^6	62.10
E_{meth}	$kJ\ mol^{-1}$	76.54	179.98	E_4	$kJ\ mol^{-1}$	74.98	154.63
$k_{0,eth}$	$mol\ kg^{-1}\ s^{-1}$	2.03×10^4	223.40	$k_{0,WGS}$	$mol\ kg^{-1}\ s^{-1}$	6.89×10^5	130.64
E_{eth}	$kJ\ mol^{-1}$	125.28	49.48	E_{WGS}	$kJ\ mol^{-1}$	83.59	299.32
$k_{0,i,par}$	$mol\ kg^{-1}\ s^{-1}$	1.14×10^7	327.70	$K_1(K_{CO})$	bar^{-1}	1.78	381.40

$E_{i,par}$	$kJ\ mol^{-1}$	90.22	248.64	$K_2(K_{H_2})$	bar^{-1}	4.81×10^{-3}	230.29
$k_{0,g,par}$	$mol\ kg^{-1}\ s^{-1}$	3.04×10^{3}	95.79	$K_3(K_{HCO})$	–	5.53	356.09
$E_{g,par}$	$kJ\ mol^{-1}$	82.57	282.68	$K_6(K_{OH})$	–	5.12×10^{-2}	137.05
$k_{0,t,par}$	$mol\ kg^{-1}\ s^{-1}$	7.85×10^{3}	132.00	$K_5(K_{CH})$	–	2.19	348.80
$E_{t,par}$	$kJ\ mol^{-1}$	95.63	191.64	$K_7(K_{CH_2})$	–	4.36	301.85
$k_{0,i,olef}$	$mol\ kg^{-1}\ s^{-1}$	8.44×10^{6}	134.76	K_{W_1}	bar^{-1}	4.15×10^{-2}	367.16
$E_{i,olef}$	$kJ\ mol^{-1}$	95.34	252.90	K_{W_2}	bar^{-1}	7.84×10^{-2}	300.04
$k_{0,g,olef}$	$mol\ kg^{-1}\ s^{-1}$	7.56×10^{3}	45.04	K_{W_3}	–	2.67	390.72
$E_{g,olef}$	$kJ\ mol^{-1}$	88.31	181.78	K_{W_5}	bar	5.40×10^{1}	38.50
$k_{0,t,olef}$	$mol\ kg^{-1}\ s^{-1}$	1.75×10^{3}	75.39				
$E_{t,olef}$	$kJ\ mol^{-1}$	100.22	87.81	MAPD = 5.93%			

*Results of statistical analysis:

(i) F-test: $F_{\text{ratio}} = 921.75 > F_{critical}\ (n-m, m-1; 1-\alpha) = F_{critical}\ (144-30, 30-1; 1-0.01) = 2.14$

(ii) t-test: lowest t-value $= 38.5 > t_{critical}\ (n-m; 1-\alpha) = t_{critical}\ (144-30; 1-0.01) = 2.36$

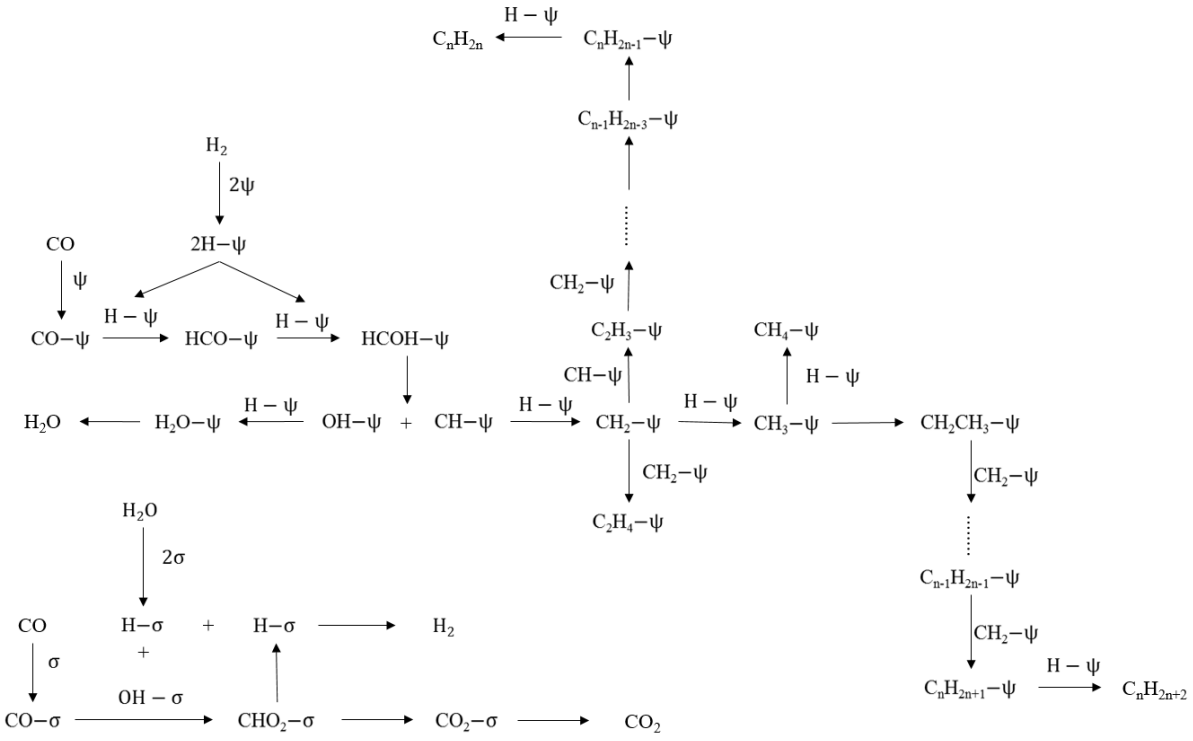

Figure 1 Reaction mechanism for the formation of paraffinic hydrocarbons (C_nH_{2n+2}) via alkyl species, olefins' products (C_nH_{2n}) via vinyl intermediates and WGS reaction via formation of formate intermediates (developed combined FT/WGS mechanism) [14].

Table 3 Reaction pathway and LHHW rate expressions developed for model FT–III based on H-assisted CO dissociation mechanism [14]

No.	General Reaction Path	Kinetic parameter	Rate Equations
1	$CO + \psi \rightleftarrows CO - \psi$	K_1	$K_1 P_{CO} \psi = \psi_{CO}$
2	$H_2 + 2\psi \rightleftarrows 2H - \psi$	K_2	$K_2 P_{H_2} \psi^2 = \psi_H^2$
3	$CO - \psi + H - \psi \rightleftarrows HCO - \psi + \psi$	K_3	$K_3 \psi_{CO} \psi_H = \psi_{HCO} \psi$
4	$HCO - \psi + H - \psi \rightleftarrows HCOH - \psi + \psi$	K_4	$K_4 \psi_{HCO} \psi_H = \psi_{HCOH} \psi$
5	$HCOH - \psi + \psi \rightleftarrows CH - \psi + OH - \psi$	K_5	$K_5 \psi_{HCOH} \psi = \psi_{CH} \psi_{OH}$
6	$OH - \psi + H - \psi \rightleftarrows H_2O + 2\psi$	K_6	$k_6 \psi_{OH} \psi_H = P_{H_2O} \psi^2$
7	$CH - \psi + H - \psi \rightleftarrows CH_2 - \psi + \psi$	K_7	$K_7 \psi_{CH} \psi_H = \psi_{CH_2} \psi$ $R_{FT} = k_{i,par} \psi_{CH_2} \psi_H$
8	$CH_2 - \psi + H - \psi \rightarrow CH_3 - \psi + \psi$	$k_{i,par}$	$\frac{d\psi_{CH_3}}{dt} = 0 \Rightarrow +R_8 - R_9 - R_{12} = 0 \Rightarrow + k_{i,par} \psi_{CH_2} \psi_H - k_{meth} \psi_{CH_3} \psi_H - k_{g,par} \psi_{CH_3} \psi_{CH_2} = 0$ $\psi_{CH_3} = \frac{k_{i,par} \psi_{CH_2} \psi_H}{k_{g,par} \psi_{CH_2} + k_{meth} \psi_H}$
9	$CH_3 - \psi + H - \psi \rightarrow CH_4 + 2\psi$	k_{meth}	$R_{CH_4} = k_{meth} \psi_{CH_3} \psi_H$
10	$CH_2 - \psi + CH_2 - \psi \rightarrow C_2H_4 + 2\psi$	k_{eth}	$R_{C_2H_4} = k_{eth} \psi_{CH_2}{}^2$
11	$CH_2 - \psi + CH - \psi \rightarrow C_2H_3 - \psi + \psi$	$k_{i,olef}$	$\frac{d\psi_{C_2H_3}}{dt} = 0 \Rightarrow +R_{11} - R_{14} = 0 \Rightarrow + k_{i,olef} \psi_{CH_2} \psi_{CH} - k_{g,olef} \psi_{CH_2} \psi_{C_2H_3} = 0$ $\psi_{C_2H_3} = \frac{k_{i,olef} \psi_{CH}}{k_{g,olef}}$
12	$C_{n-1}H_{2n-1} - \psi + CH_2 - \psi \rightarrow C_nH_{2n+1} - \psi + \psi\ ;\ n \geq 3$	$k_{g,par}$	$\frac{d\psi_{C_nH_{2n+1}}}{dt} = 0 \Rightarrow +R_{12} - R'_{12} - R_{13} = 0 \Rightarrow + k_{g,par} \psi_{C_{n-1}H_{2n-1}} \psi_{CH_2} - k_{g,par} \psi_{C_nH_{2n+1}} \psi_{CH_2} - k_{t,par} \psi_{C_nH_{2n+1}} \psi_H = 0$ $\psi_{C_nH_{2n+1}} = \frac{k_{g,par} \psi_{C_{n-1}H_{2n-1}} \psi_{CH_2}}{k_{g,par} \psi_{CH_2} + k_{t,par} \psi_H}$
13	$C_nH_{2n+1} - \psi + H - \psi \rightarrow C_nH_{2n+2} + 2\psi$	$k_{t,par}$	$R_{parffins} = k_{t,par} \psi_{C_nH_{2n+1}} \psi_H$
14	$CH_2 - \psi + C_{n-1}H_{2n-3} - \psi \rightarrow C_nH_{2n-1} - \psi + \psi;\ n \geq 3$	$k_{g,olef}$	$\frac{d\psi_{C_nH_{2n-1}}}{dt} = 0 \Rightarrow +R_{14} - R'_{14} - R_{15} = 0 \Rightarrow + k_{g,olef} \psi_{C_{n-1}H_{2n-3}} \psi_{CH_2} - k_{g,olef} \psi_{C_nH_{2n-1}} \psi_{CH_2} - k_{t,olef} \psi_{C_nH_{2n-1}} \psi_H = 0$ $\psi_{C_nH_{2n-1}} = \frac{k_{g,olef} \psi_{C_{n-1}H_{2n-3}} \psi_{CH_2}}{k_{g,olef} \psi_{CH_2} + k_{t,olef} \psi_H}$
15	$C_nH_{2n-1} - \psi + H - \psi \rightarrow C_nH_{2n} + 2\psi$	$k_{t,olef}$	$R_{olefins} = k_{t,olef} \psi_{C_nH_{2n-1}} \psi_H$

Table 4 Kinetic model FT–III assuming steps 4 and 8–15 are the rate-determining steps (RDS-2) [14]

No.	FT–III (RDS-2: 4, 8–15)	Rate Equations
1	$CO + \psi \rightleftarrows CO - \psi$	$\psi_{CO} = K_1 P_{CO} \psi$
2	$H_2 + 2\psi \rightleftarrows 2H - \psi$	$\psi_H = \sqrt{K_2 P_{H_2}}\,\psi$
3	$CO - \psi + H - \psi \rightleftarrows HCO - \psi + \psi$	$\psi_{HCO} = \frac{K_3 \psi_{CO} \psi_H}{\psi} = \frac{K_3 K_1 P_{CO} \psi \sqrt{K_2} P_{H2}^{0.5} \psi}{\psi} = K_3 K_1 \sqrt{K_2} P_{CO} P_{H2}^{0.5} \psi$
4	$HCO - \psi + H - \psi \rightarrow HCOH - \psi + \psi$	$R_{FT} = k_4 \psi_{HCO} \psi_H = k_4 \left(K_3 K_1 \sqrt{K_2} P_{CO} P_{H2}^{0.5} \psi\right) \left(\sqrt{K_2 P_{H_2}}\,\psi\right) = k_4 K_1 K_2 K_3 P_{CO} P_{H_2} \psi^2$
5	$HCOH - \psi + \psi \rightleftarrows CH - \psi + OH - \psi$	$\psi_{HCOH} = \frac{\psi_{OH} \psi_{CH}}{K_5 \psi} = \frac{\left(\frac{P_{H_2O}}{K_6 \sqrt{K_2 P_{H_2}}} \psi\right) \left(\frac{k_4 K_1 K_2^{0.5} K_3}{k_{i,par} K_7} P_{CO} P_{H_2}^{0.5} \psi\right)}{K_5 \psi} = \frac{k_4 K_1 K_3}{k_{i,par} K_5 K_6 K_7} P_{H_2O} P_{CO} \psi$
6	$OH - \psi + H - \psi \rightleftarrows H_2O + 2\psi$	$\psi_{OH} = \frac{\psi^2 P_{H_2O}}{K_6 \psi_H} = \frac{\psi^2 P_{H_2O}}{K_6 \sqrt{K_2 P_{H_2}} \psi} = \frac{P_{H_2O}}{K_6 \sqrt{K_2 P_{H_2}}} \psi$
7	$CH - \psi + H - \psi \rightleftarrows CH_2 - \psi + \psi$	$\psi_{CH} = \frac{\psi_{CH_2} \psi}{K_7 \psi_H} = \frac{\left(\frac{R_{FT}}{k_{i,par} \psi_H}\right) \psi}{K_7 \psi_H} = \frac{R_{FT}}{K_7 k_{i,par} \psi_H^2} \psi = \frac{k_4 K_1 K_2 K_3 P_{CO} P_{H_2} \psi^2}{K_7 k_{i,par} K_2 P_{H_2} \psi^2} \psi = \frac{k_4 K_1 K_2^{0.5} K_3}{k_{i,par} K_7} P_{CO} P_{H_2}^{0.5} \psi$
8	$CH_2 - \psi + H - \psi \rightarrow CH_3 - \psi + \psi$	$R_{FT} = k_{k_{i,par}} \psi_{CH_2} \psi_H$ $\psi_{CH_2} = \frac{R_{FT}}{k_{i,par} \psi_H} = \frac{k_4 K_1 K_2 K_3 P_{CO} P_{H_2} \psi^2}{k_{i,par} \sqrt{K_2 P_{H_2}} \psi} = \frac{k_4 K_1 K_2^{0.5} K_3}{k_{i,par}} P_{CO} P_{H_2}^{0.5} \psi$
Total Surface Coverage	$\psi + \psi_{CO} + \psi_H + \psi_{OH} + \psi_{HCO} + \psi_{HCOH} + \psi_{CH} + \psi_{CH_2} = 1$	$\psi = \frac{1}{\left(\begin{array}{c} 1 + K_1 P_{CO} + \sqrt{K_2 P_{H_2}} + \frac{P_{H_2O}}{K_6 \sqrt{K_2 P_{H_2}}} + K_3 K_1 \sqrt{K_2} P_{CO} P_{H2}^{0.5} + \\ \frac{k_4 K_1 K_3}{k_{i,par} K_5 K_6 K_7} P_{H_2O} P_{CO} + \frac{k_4 K_1 K_2^{0.5} K_3}{k_{i,par} K_7} P_{CO} P_{H_2}^{0.5} + \frac{k_4 K_1 K_2^{0.5} K_3}{k_{i,par}} P_{CO} P_{H_2}^{0.5} \end{array}\right)}$

Table 5 Reaction pathway and rate equations developed based on model WGS-VII: with (RDS-4: 4) direct oxidation mechanism (formate mechanism) [14]

	WGS–VII (RDS-4: 4)	Constants	Rate Equations
1	$CO + \sigma \rightleftarrows CO - \sigma$	K_{W_1}	$\sigma_{CO} = K_{W_1} P_{CO}\, \sigma$
2	$H_2O + 2\sigma \rightleftarrows H - \sigma + OH - \sigma$	K_{W_2}	$\sigma_{OH} = \frac{K_{W_2} P_{H2O}}{\sigma_H}\sigma^2 = \frac{K_{W_2} P_{H2O}}{\sqrt{\frac{P_{H2}}{K_5}}\sigma}\sigma^2 = K_{W_2} K_5^{0.5} \frac{P_{H2O}}{P_{H2}^{0.5}}\sigma$
3	$CO - \sigma + OH - \sigma \rightleftarrows CHO_2 - \sigma + \sigma$	K_{W_3}	$\sigma_{CHO2} = \frac{K_{W_3}\sigma_{CO}\sigma_{OH}}{\sigma} = \frac{K_{W_3}\left(K_{W_1} P_{CO}\, \sigma\right)\left(K_{W_2} K_5^{0.5} \frac{P_{H2O}}{P_{H2}^{0.5}}\sigma\right)}{\sigma} = K_{W_3} K_{W_1} K_{W_2} K_{W_5}^{0.5} \frac{P_{H2O}\, P_{CO}}{P_{H2}^{0.5}}\sigma$
			$R_{WGS} = k_{WGS_4}\sigma_{CHO2} - k_{WGS_{-4}} P_{CO_2}\sigma_H = k_{WGS_4} K_{W_3} K_{W_1} K_{W_2} K_{W_5}^{0.5} \frac{P_{H2O}\, P_{CO}}{P_{H2}^{0.5}}\sigma - k_{WGS_{-4}} P_{CO_2}\sqrt{\frac{P_{H2}}{K_{W_5}}}\sigma$
4	$CHO_2 - \sigma \rightleftarrows H - \sigma + CO_2$	k_{WGS_4}	$R_{WGS} = \frac{\left(k_{WGS_4} K_{W_3} K_{W_1} K_{W_2} K_{W_5}^{0.5} \frac{P_{H_2O}\, P_{CO}}{P_{H_2}^{0.5}} - k_{WGS_{-4}} P_{CO_2}\sqrt{\frac{P_{H_2}}{K_{W_5}}}\right)}{\left(1 + K_{W_1} P_{CO} + \sqrt{\frac{P_{H_2}}{K_{W_5}}} + K_{W_3} K_{W_1} K_{W_2} K_{W_5}^{0.5} \frac{P_{H_2O}\, P_{CO}}{P_{H_2}^{0.5}} + K_{W_2} K_{W_5}^{0.5} \frac{P_{H_2O}}{P_{H_2}^{0.5}}\right)}$
5	$2H - \sigma \rightleftarrows H_2 + 2\sigma$	K_{W_5}	$\sigma_H = \sqrt{\frac{P_{H2}}{K_{W_5}}}\sigma$
Total Surface Coverage	$\sigma + \sigma_{CO} + \sigma_H + \sigma_{CHO2} + \sigma_{OH} = 1$		$\sigma = \frac{1}{\left(1 + K_{W_1} P_{CO} + \sqrt{\frac{P_{H2}}{K_{W_5}}} + K_{W_3} K_{W_1} K_{W_2} K_{W_5}^{0.5} \frac{P_{H2O}\, P_{CO}}{P_{H2}^{0.5}} + K_{W_2} K_{W_5}^{0.5} \frac{P_{H2O}}{P_{H2}^{0.5}}\right)}$

2.4. Multi-Objective Optimization Methodology

The performance of the reactor is characterized not by one but by several parameters such as reactant conversions as well as products' selectivities. Thus, such a feature requires multi-objective (opposed to single-objective) optimization of all performance parameters. Such an optimization problem is often complex especially if the objective functions (*OF*) are conflicting with respect to each other. These problems give rise to a set of trade-off optimal solutions, popularly known as Pareto-optimal solutions [41]. Therefore, due to the diversity in solutions, these problems can be solved effectively using evolutionary algorithms which utilize a population search approach and results are a group of optimal solutions rather than a single solution.

Among the evolutionary optimization algorithms, the genetic algorithm (GA) is one of the most efficient approaches. The GA is based on the biological evolution and it is started with the creation of an initial population whose elements are randomly selected in the whole design space. Different procedures are then applied in order to successively generate a new population containing better elements. The performance of an individual is measured by its fitness. Pairs of individuals are selected from this population based on their objective function values. Then each pair of individuals undergoes a reproduction mechanism to generate a new population in such a way that fitter individuals will spread their genes with higher probability. The children replace their parents and as this proceeds, inferior traits in the pool die out due to the lack of reproduction. At the same time, strong traits tend to combine with other strong traits to produce children who perform better. This procedure is repeated for the next generation until the maximum specified number of generations is reached i.e. 5000 generations (see Table 6).

Table 6 Main control operators considered in the multi-objective optimization process using NSGA–II

	Number of population	Number of generation	Crossover	Mutation rate
Values tried	100 300 400 500	5000	0.8	0.2
	500	1000 3000 4000 5000	0.8	0.2
	500	5000	0.4 0.6 0.8 0.9	0.2
	500	5000	0.8	0.001 0.01 0.1 0.2
Best values	500	5000	0.8	0.2

The GA can deal with complex optimization problems such as multi-dimensional, non-continuous, and non-linear problems. Moreover, the GA locates the global optimal values reliably from a population of solutions,

even if many local optima exist and prevents the convergence to sub-optimal solutions. This distinguishes the GA from the traditional optimization techniques that are reliant on the initial guesses; while the GA is far less sensitive to the initial conditions enforced on it. The GA will eventually reject any solution that does not show enough promise; this helps to provide more flexibility and robustness during the optimization [42].

The most common and straightforward method of defining the objective functions in multi-objective optimization problems is based on the weighted sum approach. As the name manifests, such an approach scalarizes all objective functions into a single objective, by multiplying each objective with a user-specified weight as shown by Equation 17:

$$Minimize\ or\ Maximize \qquad F(x) = \sum_{m=1}^{M} w_m f_m(x), \qquad \text{Equation 17}$$

$$Subject\ to \quad g_j(x) \geq 0 \qquad j = 1,2,\dots,J$$

$$where \quad x_i^{lower} \leq x_i \leq x_i^{upper} \qquad i = 1,2,\dots,n$$

$$0 \leq w_m \leq 1 \qquad m = 1,2,\dots.,M$$

Although simple, the outcome of the objectives' values with this approach is strongly reliant on the specified weight and also the scaling factor utilized to normalize all objective functions to the same order of magnitude.

To alleviate such deficiency, a NSGA–II (Non-dominated Sorting Genetic Algorithm-II) was employed to conduct the multi-objective optimization. The NSGA–II is an advanced version of the GA which attempts to find multiple Pareto-fronts with emphasis on non-dominated solutions and operates based on controlled elitism concepts [41]. Non-dominated solutions are the points on the first Pareto-front solution so that selecting any one of them in place of another will always sacrifice the quality of at least one objective, while improving at least one other. Such a feature is advantageous as it allows trade-off between wide ranges of optimal solutions before selecting the final one. The NSGA–II is a very fast and efficient search mechanism that utilizes crowding distance as the diversity mechanism and classifies the population into non-dominated fronts, using the Pareto-ranking approach introduced by [43]. In contrast to the weighted sum approach, in multi-objective optimization with the NSGA–II, all objectives are specified individually to be either maximized or minimized as shown in the mathematical form in Equation 18.

$$Minimize\ or\ Maximize \qquad f_m(x), \quad m = 1,2,\dots,M \qquad \text{Equation 18}$$

$$Subject\ to \quad g_j(x) \geq 0 \qquad j = 1,2,\dots,J$$

$$where \quad x_i^{lower} \leq x_i \leq x_i^{upper} \qquad i = 1,2,\dots,n$$

The weighted sum approach formulated by Equation 17 only provides the best solution corresponding to the minimum or maximum value of the single-objective function that lumps all different objectives into one objective. Therefore, it cannot provide a set of alternative solutions for comparison of various objectives especially if they are conflicting. In contrast, the multi-objective optimization with NSGA–II is advantageous as it provides a wider range of alternative solutions and allows more flexibility during decision-making and selecting the optimal solution from the Pareto-front. Such a procedure can be performed based on higher-level information by evaluating the advantageous and drawbacks of each optimal solution from the Pareto-front. Such information depends on the variation rate of objective functions on the Pareto-front charts. Further details about NSGA-II can be found in [41, 44].

3. Results and Discussion

3.1. 1Parametric Studies Results

Prior to the optimization, it was vital to conduct comprehensive parametric studies using the developed model in order to investigate the effect of input variables (i.e. reaction temperature, total pressure, space velocity, and H_2/CO molar ratio) on the reactor's critical performance parameters (i.e. syngas conversions and products' selectivities), which are dependent variables of the model. Such parametric studies are based on variation of one input parameter in a defined range (see Table 7), while other inputs were kept constant and then plotting its effects on the performance parameters mentioned above. Such plots are then examined to identify those input parameters that have the most substantial effects on dependent variables.

Table 7 Range of variation of parameters defined for parametric study

Parameters	Reference	Unit	Temperature Effects Investigation	Pressure Effects Investigation	GHSV Effects Investigation	H_2/CO Effects Investigation
T	[11]	(*K*)	470-530	500	520	510
P	[11]	(*bar*)	15	1-30	10	10
GHSV	[11]	($Nm\ell$ *(STP)* g_{cat}^{-1} h^{-1})	7500	2400	1800-6000	4500
H_2/CO	[11]	(*mol/mol*)	2	2	2	1-3.2

3.1.1. Effects of Operating Temperature

Figure 2 shows the influences of the reaction temperature on CO and H_2 conversions, as well as the selectivities of CO_2, CH_4, and C_{5+} products at a constant total inlet pressure of 15 *bar*, H_2/CO ratio of 2 and gas hourly space velocity (GHSV) of 7500 $Nm\ell$ *(STP)* g_{cat}^{-1} h^{-1}. The effects of temperature on the light paraffinic content (i.e. C_2-C_7) of the products are illustrated in Figure 3. In addition, the product olefins as well as the changes of olefin to paraffin ratio with respect to the temperature are depicted in Figure 4. Figure 2 manifests the significant growth of the catalyst's activity and its performance upon the raising of the reaction temperature in terms of the syngas components' conversion, suggesting that the temperature has positive effects on CO and H_2 conversion in which both quantities increase substantially from about 35% to 92% and 35% to 74% respectively, by increasing the

temperature from 470 *K* to 530 *K*. The undesired CO_2 selectivity increases from about 0.04% to 13% upon the rising of the temperature. From Figure 2 to Figure 4, one can conclude that the increment of temperature results in a shift towards products with low molecular weight hydrocarbons on a Co/SiO_2 catalyst i.e. methane, olefins: C_2-C_3, paraffins: C_2-C_7. It is apparent that the formation of heavier hydrocarbons (C_{5+}) is favoured at lower temperatures; while at high temperatures, the reactor produces higher low molecular weight products (see Figure 2 to Figure 4). The total light hydrocarbon products with carbon atoms between C_2-C_7 increases from 2.75% to 10.31% and there are increases of methane from 3.7% to 20.3%, while the selectivity of C_{5+} decreases substantially from about 94% to 71%. Also, the results justify the decrease of the low molecular weight olefin to paraffin ratio upon increasing the temperature (see Figure 4). Hence, low temperatures favour the higher formation of heavy liquid products, the lower undesired CH_4 and CO_2 selectivities, as well as a higher olefin to paraffin ratio. In contrast, high temperatures are desirable to increase the conversion of syngas components (CO and H_2), the paraffin to olefin ratio, and for the production of light hydrocarbons, especially CH_4.

Moazami *et al.* [14] showed that the methane has a higher temperature dependency compared to other hydrocarbons due to its lower activation barriers. As expected, methane and desired heavier hydrocarbons had opposite variations with respect to temperature change. The question is why the effects of temperature on outlet liquid phase selectivity are different from methane selectivity and syngas conversion. As depicted in Figure 2, the positive effects of temperature on syngas conversion is due to the nature of the Arrhenius expression and reaction rate since both are temperature dependent and positively impact the conversion; all the reactions are enhanced with a greater temperature so more reactants are consumed. However, products' distribution is not directly proportional to the temperature. This can be explained by the nature of the chain growth probability (α). Indeed, α is defined by the rate of propagation (growth) and termination steps through Equation 19. Also, mole fraction, y_n, with n carbon atom number is equated to α through Equation 20. It is worth noting that when the value of alpha is high, it is proportional to y_n ($\alpha \propto y_n$). The α value is in the range of 0 to 1 and is closer to 1 when the desired FT products are heavy hydrocarbons. On the other hand, α is inversely proportional to the termination reaction rate (R_t), and that all reaction rates (e.g. R_g, R_t, and etc.) increases upon the increasing of the temperature. Therefore, at higher temperatures, the chain growth probability (considering heavy FT products) value would be lower, suggesting that the alpha value is inversely proportional to the temperature ($\alpha \propto 1/T$) and with the lower alpha value the mole fraction would be lower as well. This can justify why the increase of temperature decreases the selectivity of the liquid product, while that of light hydrocarbons grows. In other words, from the very different values of the activation energies (see Table 2), the C_{5+} products' formation is noticeably favoured over that of the light hydrocarbons upon the decrease of reaction temperature.

To sum up, the increase of temperature increases the rate constants and all reaction rates (through the Arrhenius equation), followed by the decrease of chain growth probability; therefore, this results in the decrease of the mole fraction of the liquid content of the products. The olefin to paraffin ratio can also be explained by the same reason and considering the greater reaction rate for the termination step of the paraffinic compounds ($R_{t,par}$) compared to that of the olefins ($R_{t,olef}$) due to lower activation energy barriers of the former compared to the latter (see Table 2). The lower activation barriers of the former causes the termination reaction rate to grow faster

with an increase of temperature compared to the latter. Assuming a separate alpha value for paraffins (α_P) and olefins (α_O), the denominator of Equation 19 would be greater for α_P than that of the olefins, implying higher α_O compared to that of paraffins. Therefore, the mole fraction of the olefins would increase faster than for paraffins. In contrast to heavier hydrocarbon, the y_n value for lighter hydrocarbons has inverse proportionality to α value. In this case, since the α_O/α_P ratio increases upon the increment of reaction temperature, hence the y_O/y_P decreases due to their inverse proportionality. This justifies why the increase of temperature decreases the selectivity the olefins to paraffins ratio.

$$\alpha = \frac{R_g}{R_g + R_t} \qquad \text{Equation 19}$$

$$y_n = (1-\alpha)\alpha^{n-1} \qquad \text{Equation 20}$$

Figure 5 indicates how the CO and H_2 conversions and mole fractions at the centreline of the reactor are influenced by the reaction temperature when the process conditions are set at constant total pressure of 25 *bar*, H_2/CO ratio of 2 and at high space velocity of 4500 $Nm\ell$ *(STP)* g_{cat}^{-1} h^{-1} (Figure 5). From these families of figures, it is apparent that the CO and H_2 mole fractions decrease, while their consumptions and conversions enhance significantly along the axial distance of the reactor bed length as the temperature rises, regardless of the syngas space velocity. Generally, these figures imply that the consumption of syngas species increases faster and their mole fraction decreases drastically upon increasing the temperature.

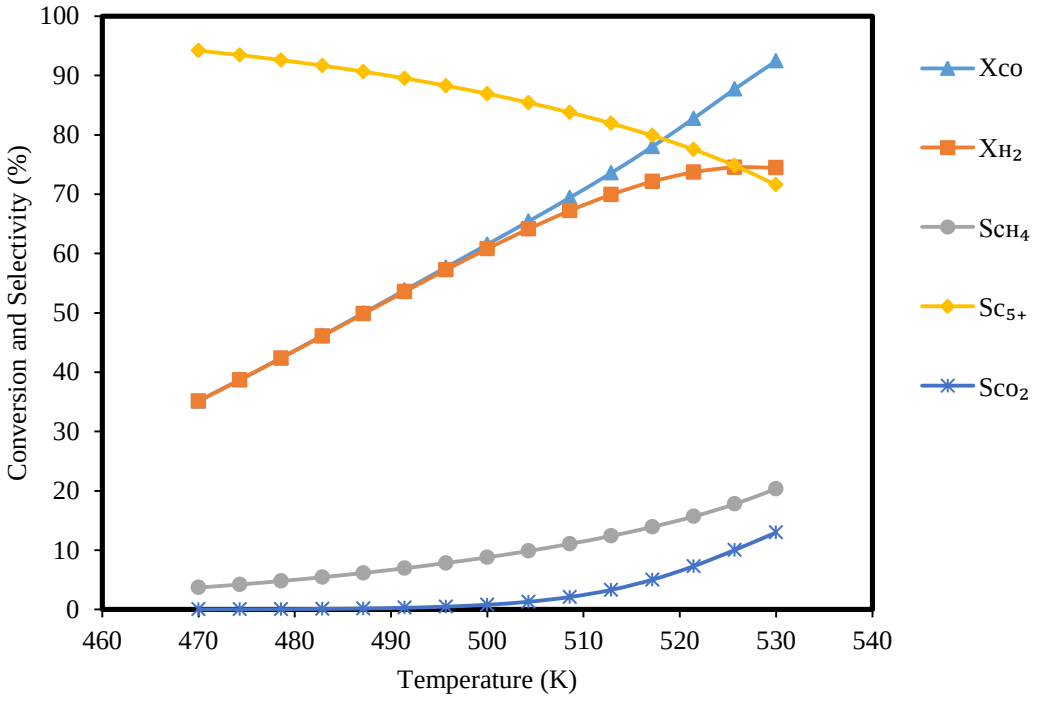

Figure 2 Effects of reaction temperatures on CO and H_2 conversions as well as the CO_2, CH_4, and C_{5+} products' selectivities at constant P = 15 *bar*, GHSV = 7500 $Nm\ell$ *(STP)* g_{cat}^{-1} h^{-1} and H_2/CO = 2.

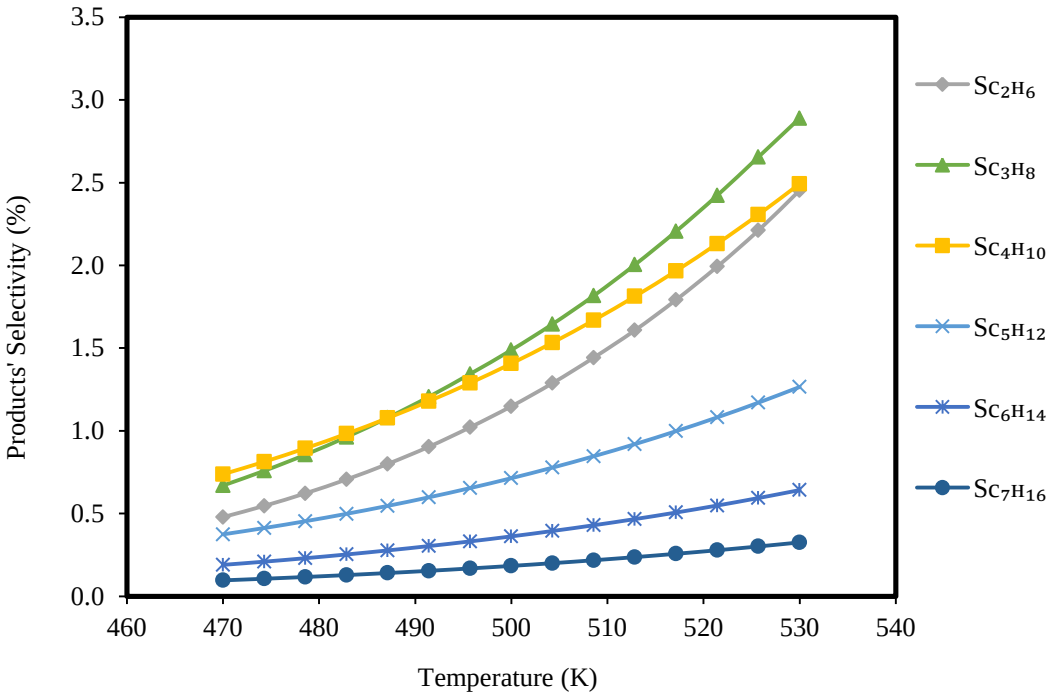

Figure 3 Effects of reaction temperature on the light paraffinic content (i.e. C_2-C_7) of the products at constant P = 15 *bar*, GHSV = 7500 $Nm\ell\ (STP)\ g_{cat}^{-1}\ h^{-1}$ and $H_2/CO = 2$.

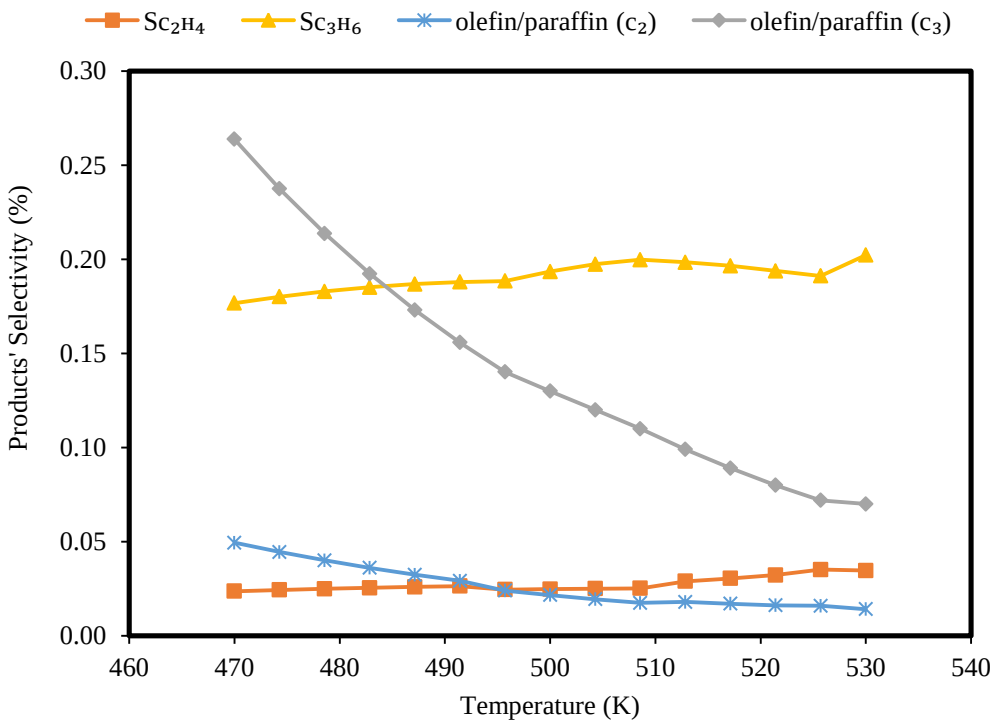

Figure 4 Effects of reaction temperature on the product olefins as well as the changes of olefin to paraffin ratio at constant P = 15 *bar*, GHSV = 7500 $Nm\ell\ (STP)\ g_{cat}^{-1}\ h^{-1}$ and $H_2/CO = 2$.

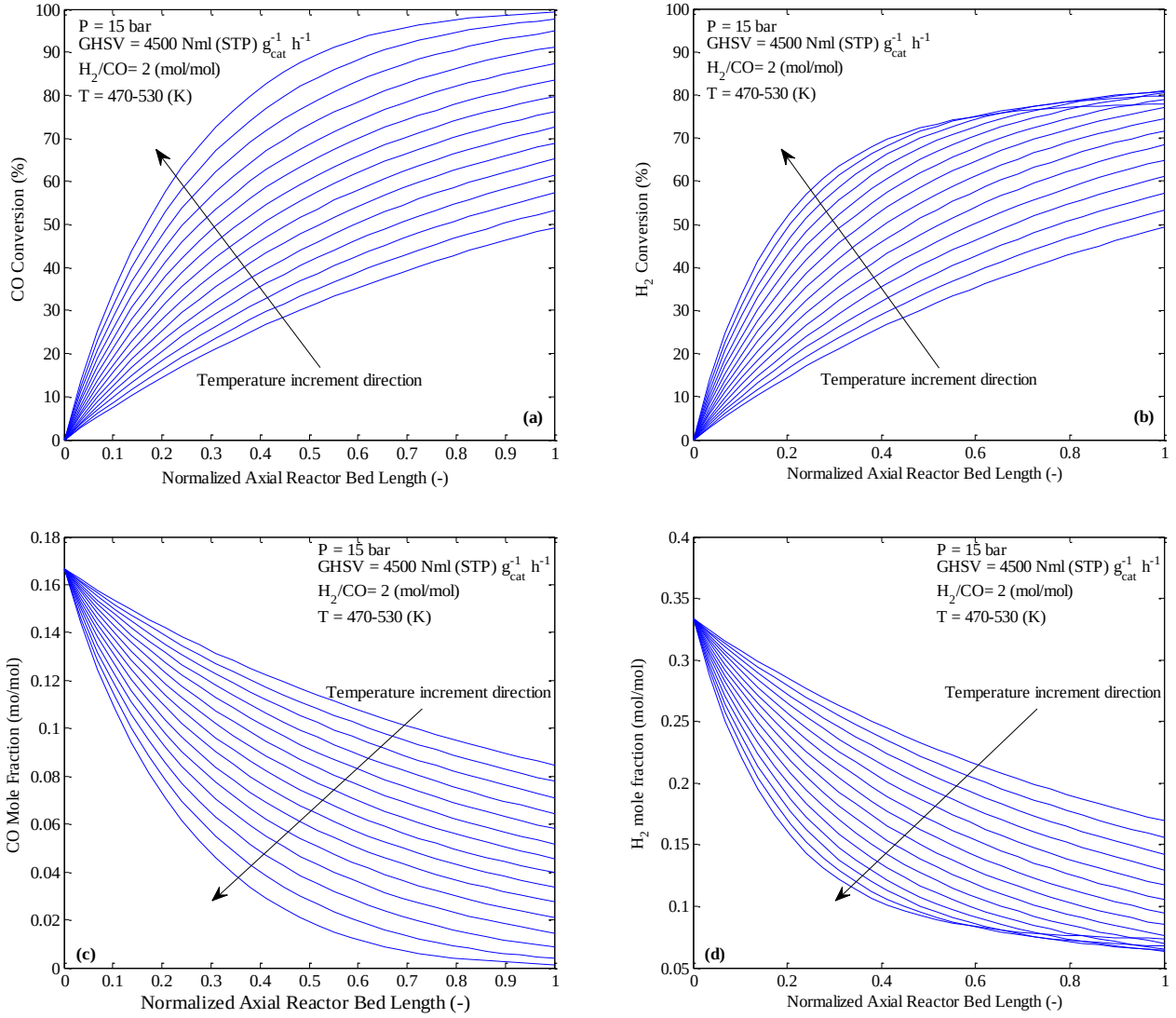

Figure 5 The changes of conversion of (a) CO and (b) H_2 and mole fraction of the same species (c) and (d) respectively along the normalized axial dimension of the reactor bed length, effects of temperatures on their behaviour at constant P = 15 *bar*, GHSV = 4500 $Nm\ell\ (STP)\ g_{cat}^{-1}\ h^{-1}$ and $H_2/CO = 2$.

3.1.2. **Effects of Operating Space Velocity**

The changes of CO and H_2 conversions, as well as, selectivities of CO_2, CH_4 and C_{5+} under different process conditions with respect to gas hourly space velocity (GHSV) on a Co/SiO_2 catalyst are illustrated in Figure 6. This study was performed at the constant reaction temperature, total inlet pressure, and H_2/CO molar ratio listed in Table 7.

From Figure 6, the highest conversion of both CO and H_2 were obtained at the lowest GHSV in the range of the studied process conditions. In fact, a low GHSV is associated with a high residence time so that the reactants have sufficient time to react and their concentrations subsequently decrease; this justifies that the CO and H_2 conversions increases upon decreasing the space velocity.

In addition, the results manifest the substantial increase of selectivity of heavy products and the decrease of that of methane upon increasing the space velocity, suggesting that the increase of space velocity leads to the elimination of mass transfer resistance so that the dominant effects of diffusional limitation yield the removal of hydrocarbons from the active sites at the surface of the catalyst. Therefore, the increase of GHSV favours the production of long chain heavy hydrocarbon components, while CH_4 selectivity, as expected, goes in the opposite direction. The heavy products' selectivity increases from about 58% to 83% with the increasing of the GHSV from 1800 to 6000 $Nm\ell\ (STP)\ g_{cat}^{-1}\ h^{-1}$; whereas the undesired methane selectivity decreases from about 35% to 10%. The lighter olefins (C_2-C_3) and paraffins (C_2-C_7) were nearly unchanged considering significant changes of space velocity in the range of 1800-6000 $Nm\ell\ (STP)\ g_{cat}^{-1}\ h^{-1}$. In general, the results show that the selectivities of heavy FT products were sensitive to space velocity changes on a Co/SiO_2 catalyst, while this parameter was the key element to attain the high conversion (CO and H_2) rates; hence, likewise the temperature factor had a significant impact on the catalytic activity, reaction kinetics and general performance of the reactor.

Figure 7 indicates the changes of CO and H_2 conversions and mole fractions in the gaseous phase respectively, at the centreline of the reactor bed versus normalized axial distance of the reactor bed length for different values of GHSV changing from 1800 to 6000 $Nm\ell\ (STP)\ g_{cat}^{-1}\ h^{-1}$. The figure includes a family curves for different space velocity. Figure 7 represents the results obtained at a temperature of 490 *K*. The results indicate that the CO and H_2 consumptions are more sensitive to GHSV for the lower temperature's case. For instance, the increase of GHSV from 1800 to 6000 $Nm\ell\ (STP)\ g_{cat}^{-1}\ h^{-1}$ results in the reduction of CO and H_2 conversions from 82% and 83% to 51% and 53% at the lower temperature of 490 *K*, respectively; whereas, the similar variables decrease from 99% and 82% to 81% and 73% respectively, at the higher temperature of 520 *K*.

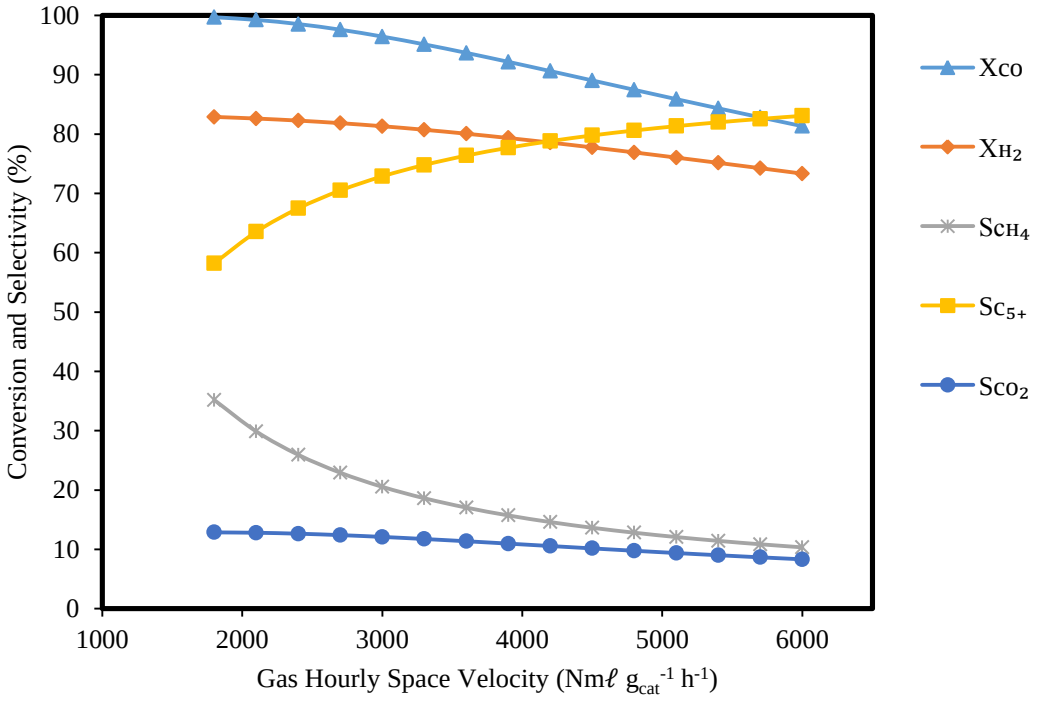

Figure 6 Effects of space velocity on CO and H_2 conversions as well as the CO_2, CH_4 and C_{5+} products' selectivities at constant P = 10 *bar*, H_2/CO = 2 and T = 520 *K*.

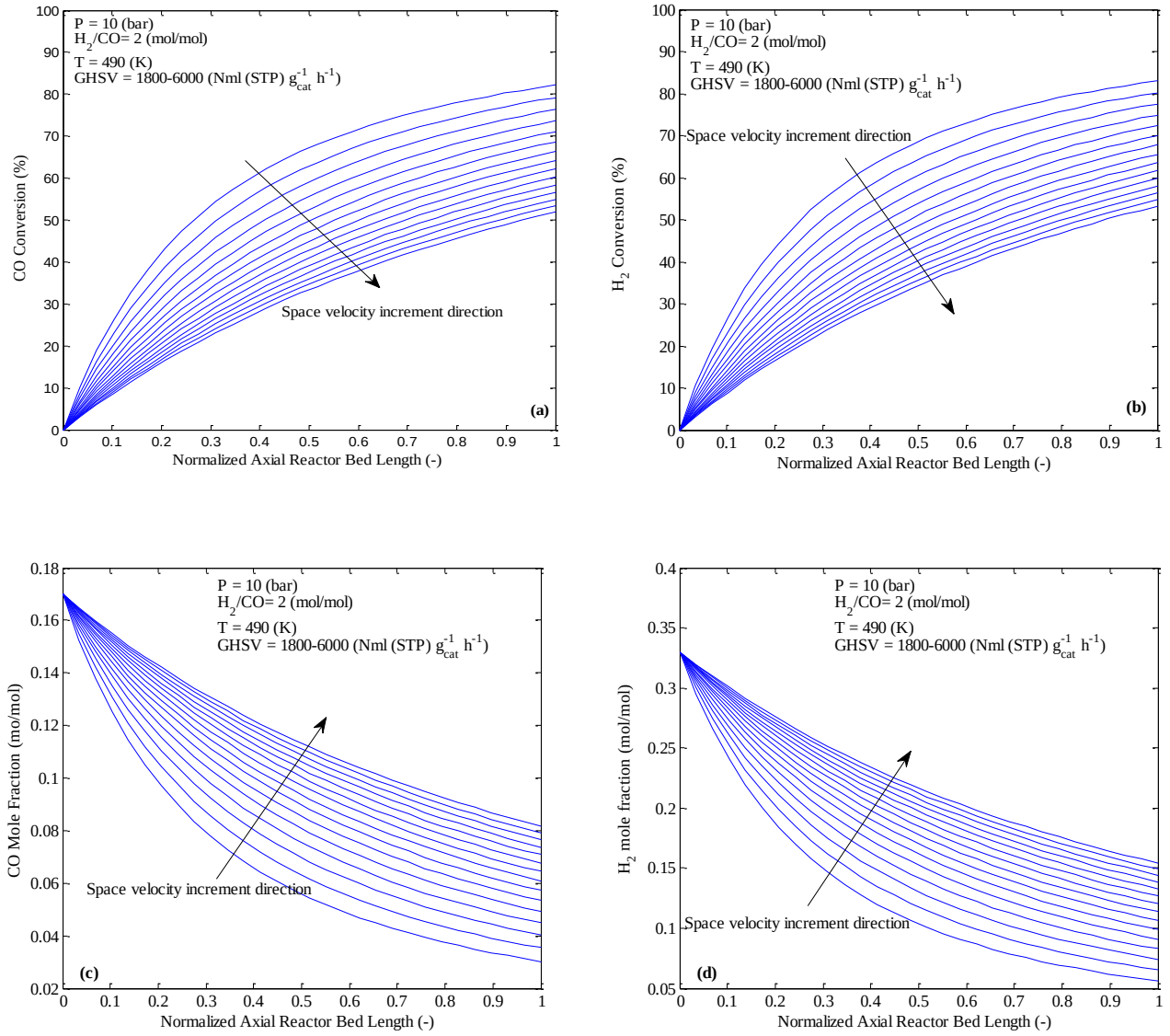

Figure 7 The changes of conversion of (a) CO and (b) H_2 and mole fraction of the same species (c) and (d) respectively along the normalized axial dimension of the reactor bed length, effects of GHSV on their behaviour at constant P= 10 *bar*, T= 490 *K* and H_2/CO= 2.

3.1.3. **Effects of Operating Pressure**

Figure 8 to Figure 10 manifest the pressure effects on syngas conversion as well as CO_2, CH_4 and C_{5+} products' selectivities, the selectivity of light paraffins, and the olefin to paraffin ratio as well as light olefin products, respectively. Typically, at low total pressures, the establishment of the thermodynamic equilibrium proceeds more gradually; whereas at equilibrium condition the products are mainly liquids. As shown in Figure 8, an increase in total pressure yields the product selectivities towards heavy products implying the condensation of hydrocarbons, which are normally in the gaseous state at atmospheric pressure. It is also important to notice that higher pressures typically lead to saturation of catalyst pores by liquid formation. From Figure 8, it is apparent that when the total pressure increases from 1 to 30 *bar*, the liquid products' selectivity significantly rises from about 36% to 92% at typical process conditions with respect to temperature, space velocity and H_2/CO molar ratio. As depicted in Figure 8, the changes of CO and H_2 conversions are proportional to the total pressure: increasing pressure results in the increment of CO and H_2 conversions from about 39% and 38% at 1 *bar* to 95% and 91% at 30 *bar*, respectively. Also, the selectivity C_2-C_7 paraffins decreases as the total pressure increases (see Figure 9). For instance, the selectivity of C_7H_{16} (heptane) decreases from 0.57% to 0.02% as the total pressure varies from 1 to 30 *bar*. Similarly, the selectivity of C_2H_6 (ethane) and C_3H_8 (propane) decrease from 3.49% and 4.15% to 0.12% and 0.14% respectively, which indicate the faster reduction of the hydrocarbon compounds with lower carbon atom number. Therefore, the increase of the total pressure would have adverse effect on tail gas and LPG productions which exhibits the increase of pressure condition is not desirable if the low chain hydrocarbons are preferable products. Similar behaviours were attained for light olefin components as it can be seen in Figure 10; whereas the olefins to paraffins ratio were not changed. CH_4 selectivity decrease substantially with the increasing of the pressure, which is a favourable condition as this component is undesired FT products.

Figure 11 and Figure 12 indicate the influence of total pressure on syngas consumptions in terms of CO and H_2 conversions and mole fractions, at the centreline of the fixed-bed reactor along the normalized axial dimension of the bed length, when the temperatures, space velocity and H_2/CO ratio are set at a constant 500 *K*, 2400 $Nm\ell$ *(STP)* $g_{cat}^{-1}\ h^{-1}$ and 2 (*mol*/*mol*), respectively. From Figure 11 and Figure 12, one can deduce that the increase of pressure from 1 to 30 *bar* results in significant enhancement of catalytic activity in terms of syngas consumption. The CO and H_2 conversion increase faster at lower total pressure (e.g. 1-10 *bar*) compared to that of the higher range of 10-20 *bar*; suggesting that the syngas consumption rate is more sensitive to total pressure at its lower range. When pressure increases from 1 *bar* to 10 *bar* then CO and H_2 raise from about 39% and 38% to about 85% and 82%, respectively; whereas at a higher-pressure range, these variables changes from 85% and 82% at 10 *bar* to 92% and 88% at 20 *bar*.

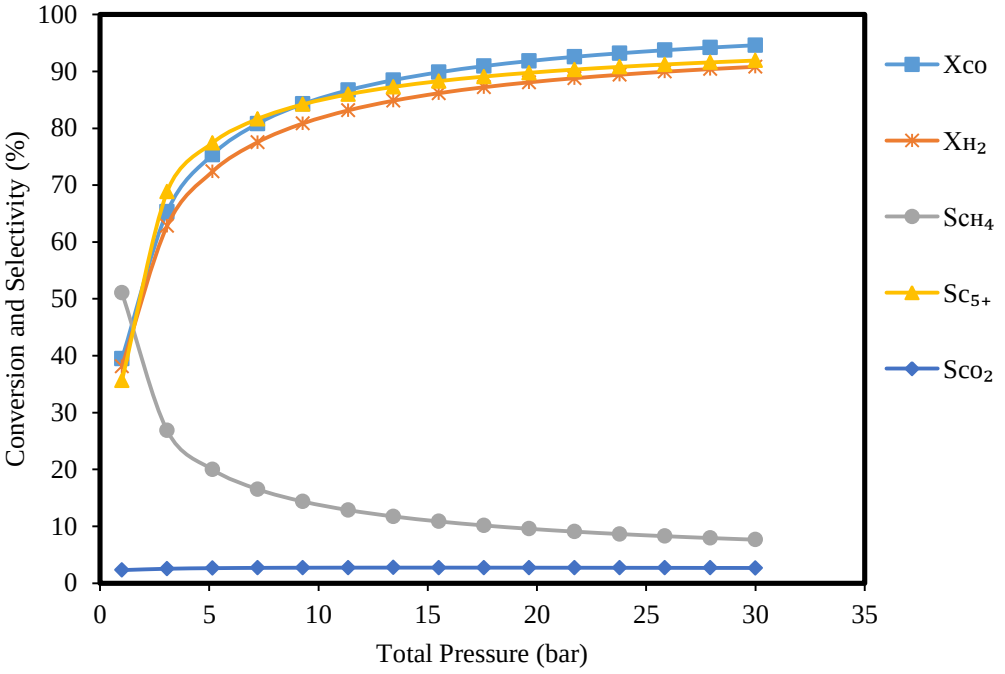

Figure 8 Effects of total pressure on CO and H_2 conversions as well as the CO_2, CH_4, and C_{5+} products' selectivities at constant T = 500 *K*, H_2/CO = 2 and GHSV = 2400 $Nm\ell\ (STP)\ g_{cat}^{-1}\ h^{-1}$.

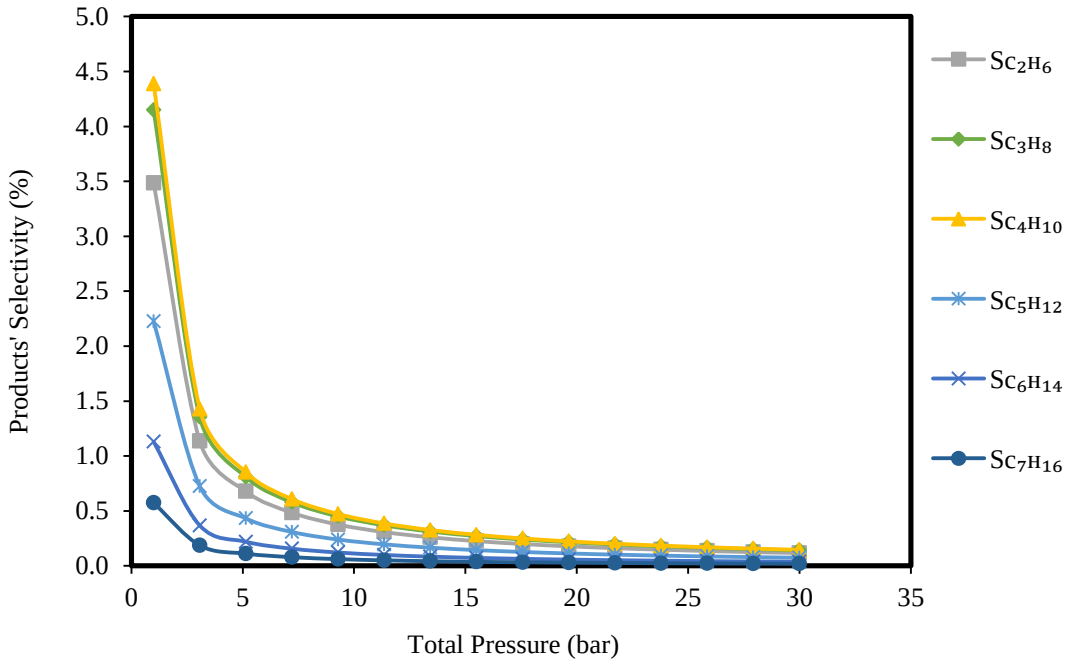

Figure 9 Effects of total pressure on the light paraffinic content (i.e. C_2-C_7) of the products at constant T = 500 *K*, H_2/CO = 2 and GHSV = 2400 $Nm\ell\ (STP)\ g_{cat}^{-1}\ h^{-1}$.

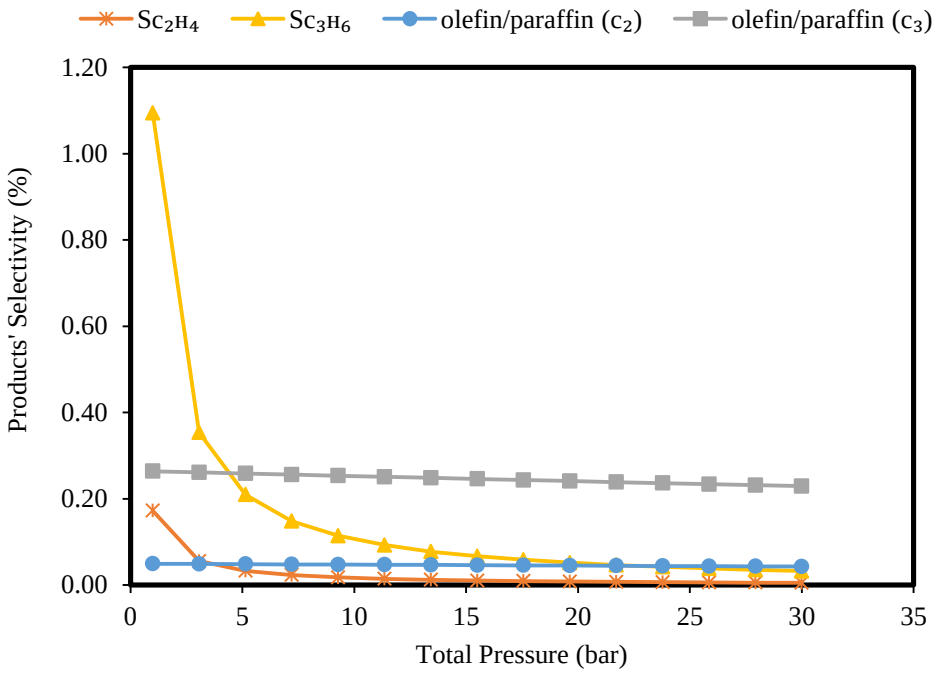

Figure 10 Effects of total pressure on the product olefins as well as the changes of olefin to paraffin ratio at constant T = 500 *K*, $H_2/CO = 2$ and GHSV = 2400 $Nm\ell\ (STP)\ g_{cat}^{-1}\ h^{-1}$.

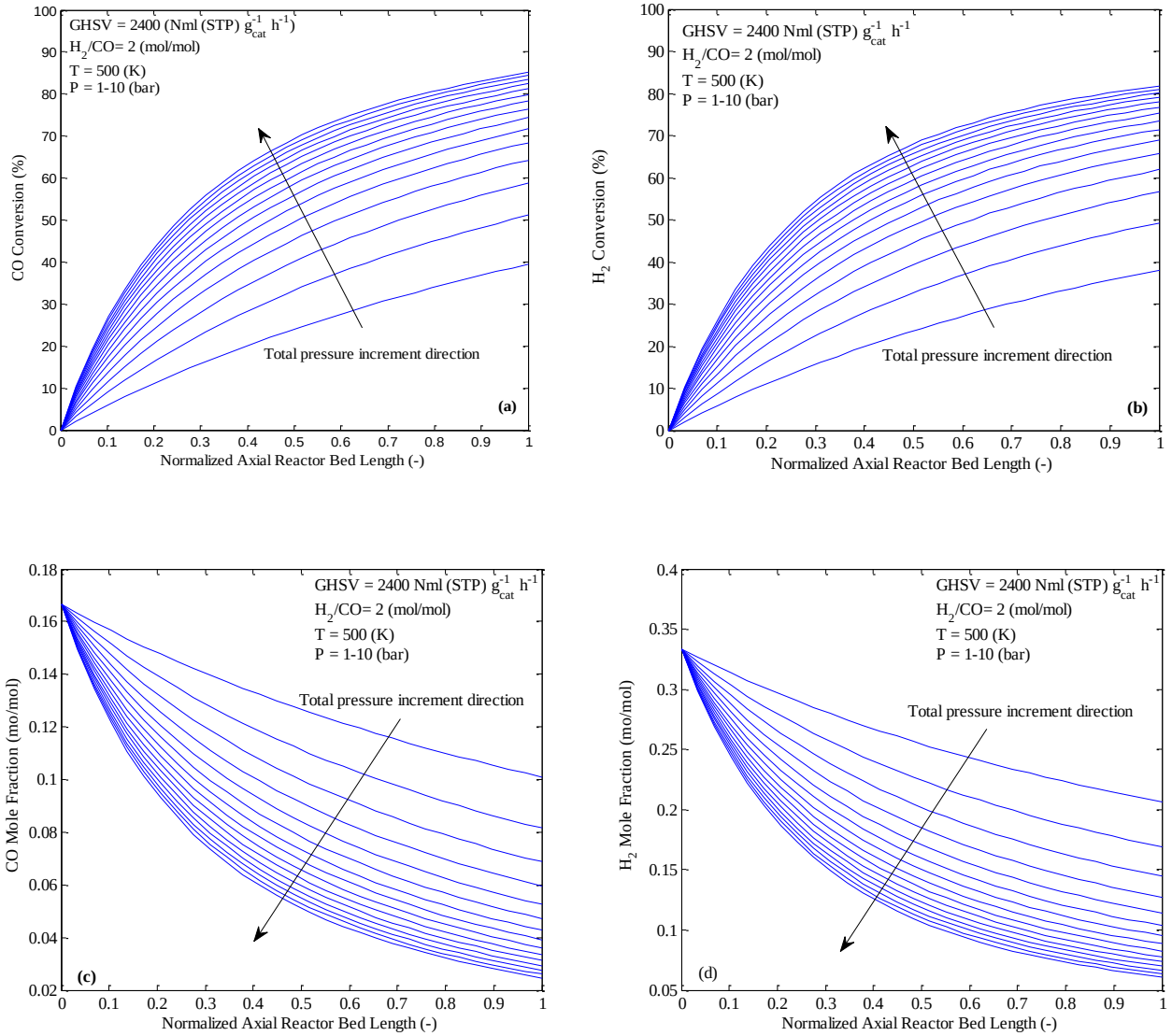

Figure 11 The changes of conversion of (a) CO and (b) H_2 and mole fraction of the same species (c) and (d) respectively along the normalized axial dimension of the reactor bed length, effects of total pressure (P =1-10 *bar*) on their behaviour at constant T = 500 *K*, GHSV = 2400 $Nm\ell\ (STP)\ g_{cat}^{-1}\ h^{-1}$ and $H_2/CO = 2$.

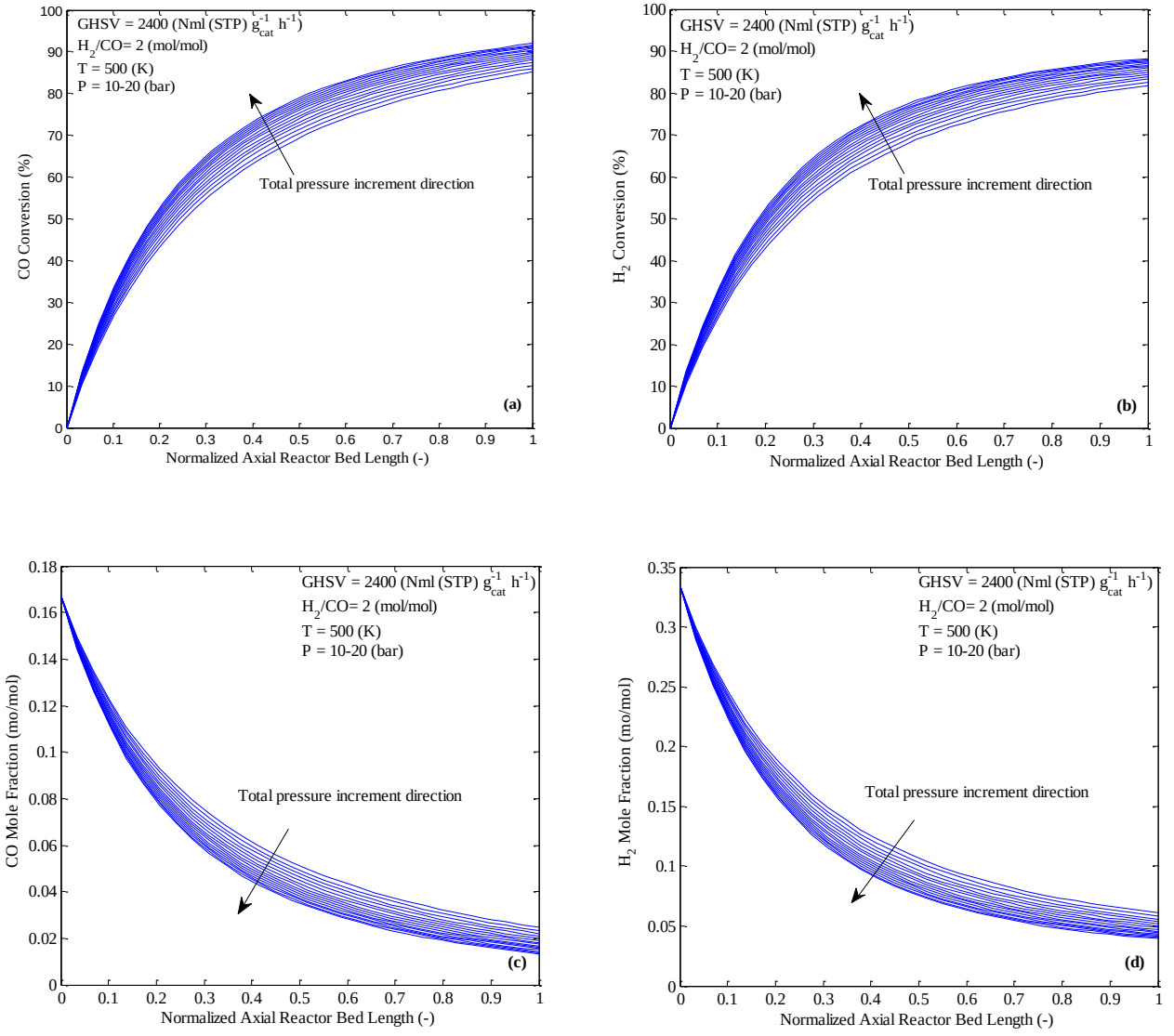

Figure 12 The changes of conversion of (a) CO and (b) H_2 and mole fraction of the same species (c) and (d) respectively along the normalized axial dimension of the reactor bed length, effects of total pressure (P =10-20 *bar*) on their behaviour at constant T = 500 *K*, GHSV = 2400 $Nm\ell\ (STP)\ g_{cat}^{-1}\ h^{-1}$ and $H_2/CO = 2$.

3.1.4. **Effects of Synthesis Gas Composition (H_2/CO Molar Ratio)**

Figure 13 shows the influence of the hydrogen to carbon monoxide molar ratio on CO and H_2 conversions, as well as the selectivities of CO_2, CH_4 and C_{5+} when the temperature, pressure and space velocity are set at 510 *K*, 10 *bar*, and 4500 $Nm\ell\ (STP)\ g_{cat}^{-1}\ h^{-1}$, respectively. Their effects on selectivities of paraffins with carbon atom C_2-C_7 are also shown in Figure 14. In addition, the product olefins as well as the changes of olefin to paraffin ratio with respect to the H_2/CO ratio are demonstrated in Figure 15. The increase of the H_2/CO ratio leads to a different proportion of adsorbed hydrogen and surface carbon atoms as well as their partial pressures. As manifested from the final developed kinetic model, CO and H_2 have inhibiting and positive impacts on the rate of reaction respectively; suggesting that the consumption rate of CO increases with the rising of the H_2/CO ratio, while that of H_2 decreases upon the increment of the ratio. The increase of the H_2/CO ratio results in the enhanced hydrogen concentration on the active sites and increments the hydrogenation degree of highly concentrated monomers. At the same time, this accelerates the rate of chain termination step causing faster desorption of products rather than incorporating to the chain growth, which results in a reduction of selectivity of heavy FT products and a subsequent increase of light hydrocarbons (C_2-C_7) (see Figure 14). It is also evident from Figure 13 that the major loss of liquid (C_{5+}) formation was due to a methanation reaction in which the C_{5+} and methane selectivities changed from about 93% to 72% and 5% to 20% with the increasing of the H_2/CO ratio from 1 to 3.5 (*mol/mol*), respectively. As can be seen in Figure 15, the olefins/paraffins ratio slightly decreases upon the increasing of the ratio, while (from Figure 13) the CO_2 selectivity decreases from about 15% to 1%; which implies the slight water gas shift activity at low H_2/CO ratio. It was found from the kinetic model and governed equations (i.e. model WGS-VII with RDS-4) that the water gas shift reaction rate is inversely proportional to the H_2/CO ratio and one can conclude that the partial pressures of both reactants as well as their proportion have substantial effects on the rate of CO_2 formation. In addition, this can be seen from Figure 16**Error! Reference source not found.** which illustrates the trend of changes of R_{WGS} (water gas shift reaction rate) along the axial dimension of the tube length at different H_2/CO molar ratio in which the rate decreases from 1.4964×10^{-5} to $1.987 \times 10^{-7}\ mol\ g_{cat}^{-1}\ s^{-1}$ upon the increasing of the molar ratio from 1 to 3.5 *mol/mol*.

Figure 17 (a) to (d) show how the CO, H_2, and syngas conversion and mole fraction at the centreline of the reactor are influenced by the input H_2/CO molar ratio when the process conditions are set at a constant temperature, pressure and GHSV of 510 *K*, 10 *bar* and 4500 $Nm\ell\ (STP)\ g_{cat}^{-1}\ h^{-1}$, respectively. In contrast to the previous figures of reactant consumption versus normalized axial distance, the inlet contents of CO mole fraction or H_2 mole fraction is not identical as the hydrogen to carbon monoxide fraction varies at the inlet of the reactor bed. From this figure, it is apparent that the increase of H_2/CO ratio leads to the increment of syngas consumption. Although this is a true manifestation, it would not be confirmed unless the comparison of syngas conversion is performed. From Figure 17, it can be deduced that the outlet CO conversion increases from 23% to 99% upon the increment of the ratio from 0.25 to 6. Overall, a high H_2/CO molar ratio would be suggested for increasing the catalytic activity and overall performance due to the considerable increase of CO conversion as well as significant reduction of CO_2 selectivity, though a low H_2/CO feed ratio would be preferable for the increased production of heavy hydrocarbons.

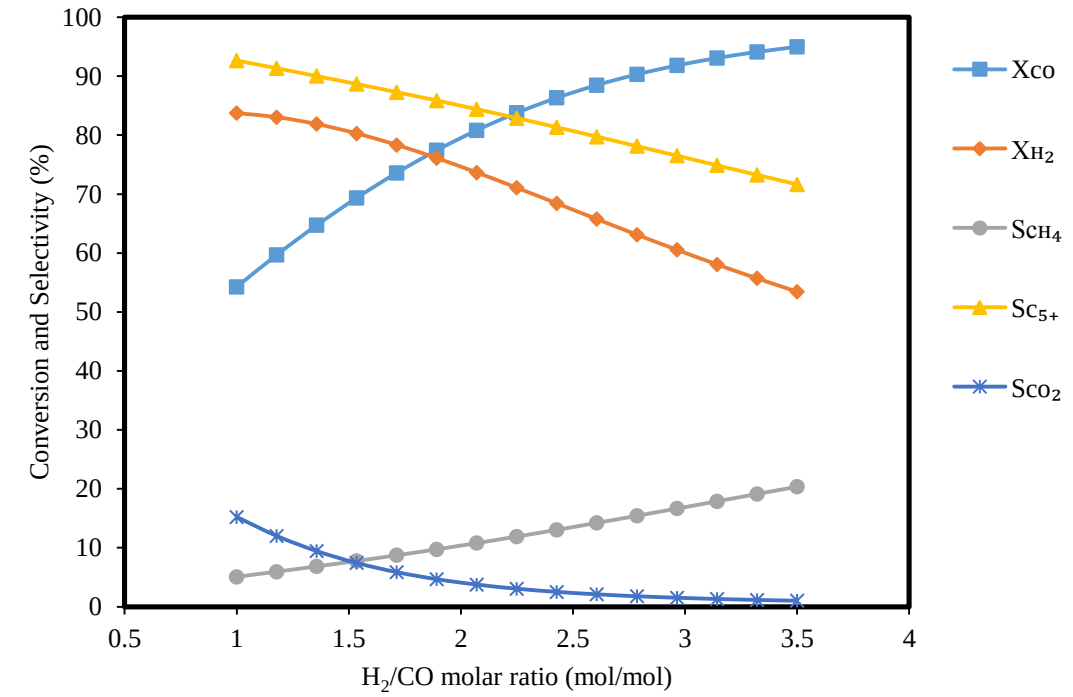

Figure 13 Effects of H_2/CO ratio on CO and H_2 conversions as well as the CO_2, CH_4, and C_{5+} products' selectivities at constant T = 510 *K*, P = 10 *bar* and GHSV = 4500 $m\ell$ *(STP)* g_{cat}^{-1} h^{-1}.

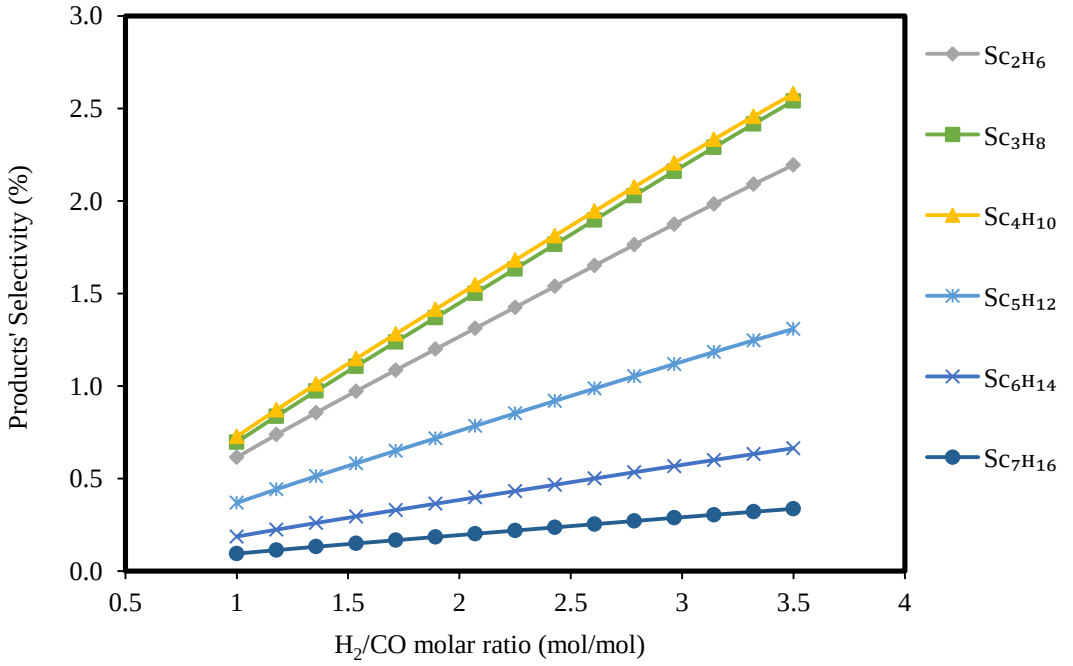

Figure 14 Effects of H_2/CO ratio on the light paraffinic content (i.e. C_2-C_7) of the products at constant T = 510 *K*, P = 10 *bar* and GHSV = 4500 $Nm\ell$ *(STP)* g_{cat}^{-1} h^{-1}.

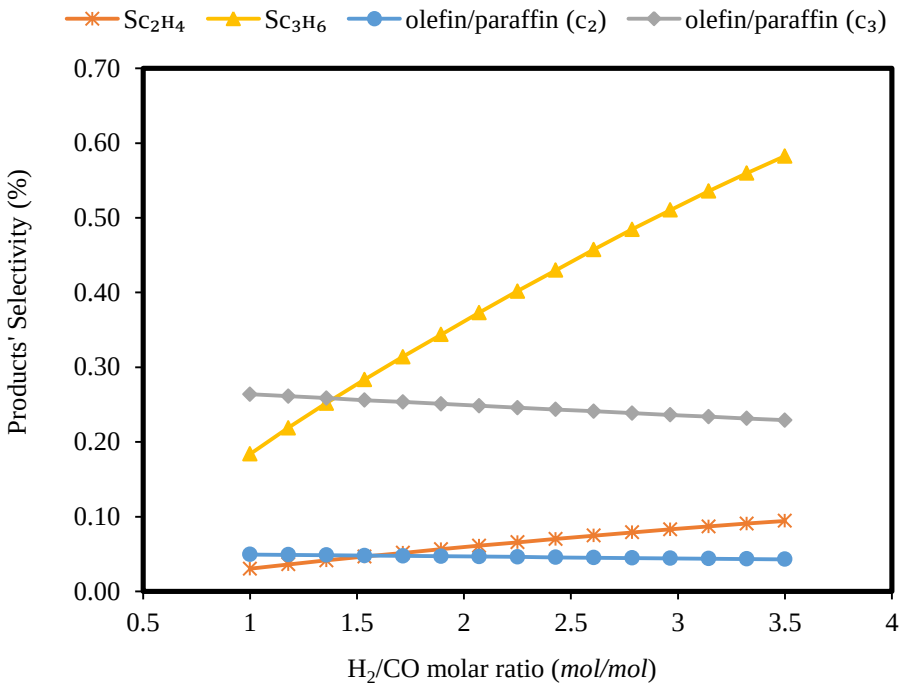

Figure 15 Effects of H_2/CO ratio on the product olefins as well as the changes of olefin to paraffin ratio at constant T = 510 *K*, P = 10 *bar* and GHSV = 4500 $Nm\ell\ (STP)\ g_{cat}^{-1}\ h^{-1}$.

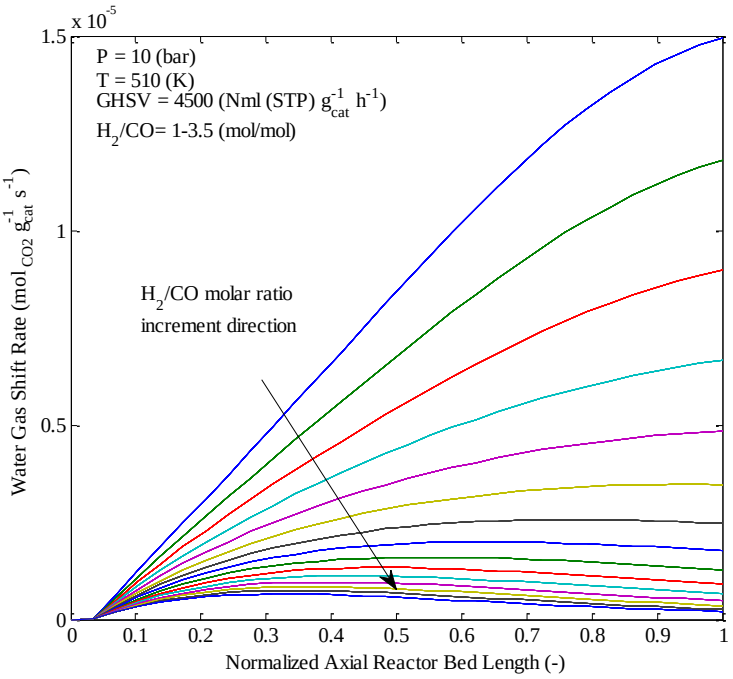

Figure 16 Effects of H_2/CO molar ratio on WGS reaction rate and its trend of changes along the normalized axial dimension of the reactor bed length, at constant T = 510 *K*, GHSV = 4500 $Nm\ell\ (STP)\ g_{cat}^{-1}\ h^{-1}$ and P = 10 *bar*.

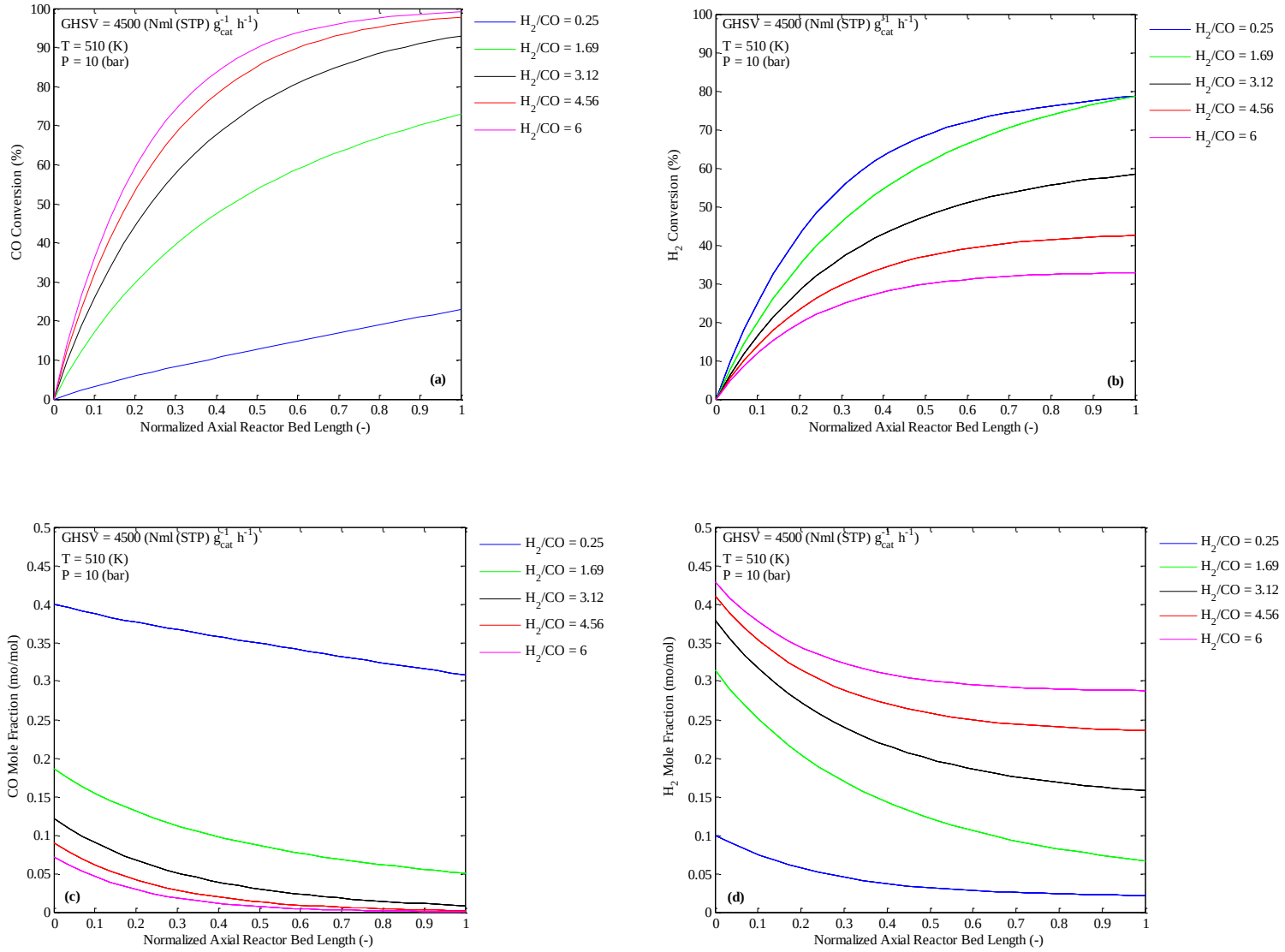

Figure 17 The changes of conversion of (a) CO and (b) H_2 and mole fraction of the same species (c) and (d) respectively along the normalized axial dimension of the reactor bed length, effects of H_2/CO on these plots at constant T = 510 *K*, GHSV = 4500 $Nm\ell\ (STP)\ g_{cat}^{-1}\ h^{-1}$ and P = 2 *bar*.

For the present study, the influences of critical process conditions i.e. reaction temperature, total pressure, space velocity, and H_2/CO inlet molar ratio on conversion of syngas compositions and FT products' selectivities, are summarized in Table 8.

Table 8 effects of operating conditions on FT products' selectivity and syngas components' conversion

Components		Temperature	Pressure	GHSV	H_2/CO molar ratio
H_2 conversion	x_{H_2}	↑	↑	↓	↓
CO conversion*	x_{CO}	↑	↑	↓	↑
CH_4 selectivity †	S_{CH_4}	↑	↓	↓	↑
CO_2 selectivity	S_{CO_2}	↑	↑§	↓	↓
Olefins selectivity	$S_{C_2-C_3}$	↑§	↓	↓§	↑
Olefin/paraffin ratio	S_O/S_P	↓	—	↓§	↓§
Light paraffins	$S_{C_2-C_7}$	↑	↓	—	↑
Liquid products	$S_{C_{5+}}$	↓	↑	↑	↓

*All the operating process conditions, except space velocity, have positive impact on CO conversion.
† The effects of all process conditions on CH_4 and C_{5+} products obtained completely in the opposite direction.
§ Slightly changed

3.2. Multi-objective Optimization Results

The obtained results, based on the parametric studies, indicated that all the process parameters had significant impacts on output conversion and products' selectivity. Hence, all parameters were considered in the multi-objective optimization process using Non-Dominated Sorting Genetic Algorithm (NSGA–II) to optimize the fitness functions (i.e. objective functions).

The target of the optimization study was to maximize the selectivity of desired products i.e. high molecular weight hydrocarbons, in general C_{5+} selectivity, to maximize the synthesis gaseous conversions (in particular CO conversion) and to minimize the formation of undesired products i.e. carbon dioxide and methane products. Accordingly, four objective functions comprised a multi-objective optimization process. Also, four control operators, as (1) the number of populations, (2) number of generations, (3) crossover and (4) mutation rate were used in the NSGA–II in which the first two were identified as the key elements. Table 6 lists the selected values of each of these operators and the best tried value of the operators in the optimization procedure. The optimizer terminates as the maximum number of generations is reached. The mutation and crossover rates were set to 0.2 and 0.8 respectively, as suggested in [42, 45]; however, different values were tried at different optimization runs to identify its impact on the optimization results. The crossover function specifies the fraction of the population at the next generation, excluding elite children, which is one of the reproduction options to specify how the genetic algorithm builds children for the succeeding generation [45]. Elite count is a positive integer specifying how many individuals in the current generation are guaranteed to survive to the next generation. The crossover enables the algorithm to extract the best genes from different individuals and recombine them into potentially superior children. Mutation adds to the diversity of a population and thereby increases the likelihood that the algorithm will generate individuals with better fitness values. More information about the operators and the method of their

selection can be found in the literature [45]. The Pareto-front solutions can be plotted by 2D and 3D scatter between two and three objectives, respectively. Figure 18 to Figure 20 show the solutions plotted by 2D scatter between CO_2 selectivity vs. CO conversion; C_{5+} selectivity vs. CO conversion; and CH_4 selectivity vs. CO conversion, respectively. One of the key factors that determines the performance of the genetic algorithm is the diversity of the population. If the average distance between individuals is large, the diversity is high; if the average distance is small, the diversity is low. Getting the right amount of diversity is a matter of trial and error. If the diversity is too high or too low, the genetic algorithm might not perform well. From (Figure 18 to Figure 20), it is apparent that the diversity of the populations are neither low nor high, which indicate that the values of crossover as well as mutation rate were perfectly defined for the current optimization; since these operators generally add to the diversity of the population and thereby increases the likelihood that the algorithm will generate individuals with better objective values [45].

The obtained Pareto frontiers reveal the conflict between the objective functions. For example, any operating conditions that increases the CO conversion will evidently reduce C_{5+} selectivity as it is apparent from Figure 19. In other words, the point of maximum CO conversion (point ‘‘A’’ in Figure 19) corresponds to the minimum of C_{5+} selectivity, while the maximum of the latter objective function leads to the minimum of the former which of course is not desirable (point ‘‘B’’ in Figure 19). If the single-objective optimization would have been conducted for CO conversion then point “A” would be the solution of the optimization, while for C_{5+} selectivity it would be point “B”. Moreover, any operating condition that increases the CO conversion increases the CH_4 selectivity which will lead to production of undesired lighter hydrocarbon compounds as can be seen from Figure 20. As it is evident, the point of maximum CO conversion (point ‘‘C’’ in Figure 20) corresponds to the maximum of CH_4 selectivity (point ‘‘D’’ in Figure 20), while the minimum of the latter objective function leads to the minimum of the former. Similarly, if the single-objective optimization would have been conducted for CO conversion then point “C” would be the solution of the optimization, while for CH_4 selectivity it would be point “D”. Apparently, there is no combination of the operating conditions that can optimize all the objectives simultaneously. Each individual point on the Pareto frontier lines in Figure 18 to Figure 20 is an optimal solution and such results can be utilized as a database of optimum solutions from which the selection of the optimum operating condition (independent variables) can be conducted from the higher-level information, experience as well as the importance of each objective function for a specific application. Comparison of the experimental data overlaid on Figure 18 to Figure 20 with Pareto-frontier solutions reveals that, not all the experiments were conducted at optimum operating conditions that led to the best performance for all objective functions. Hence, the optimization results represented herein manifested the possibility of remarkable improvement in FTS conversion and selectivities.

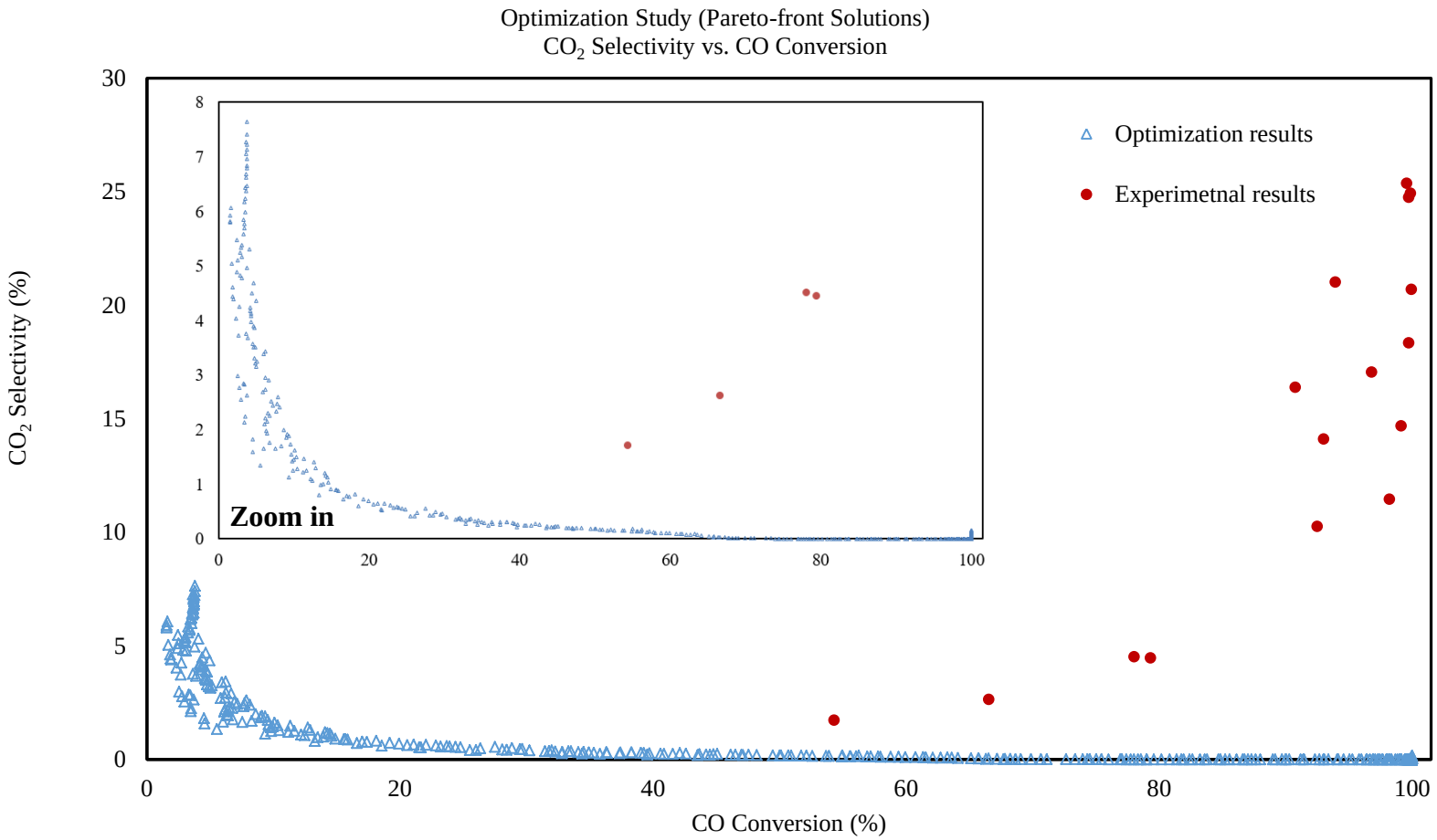

Figure 18 Pareto-front solutions obtained by optimization (between CO_2 selectivity and CO conversion) and its comparison with experimental data.

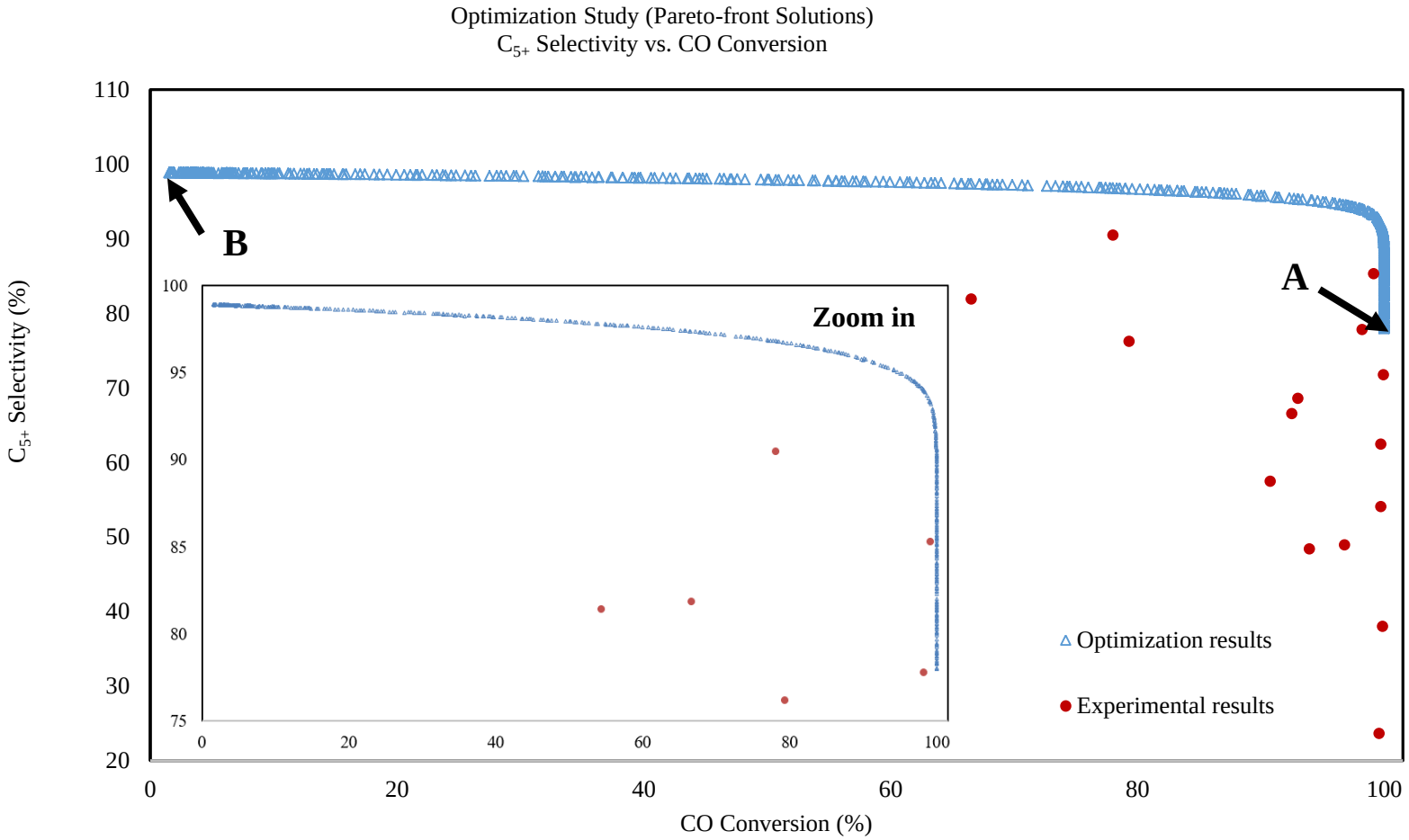

Figure 19 Pareto-front solutions obtained by optimization (between C_{5+} selectivity and CO conversion) and its comparison with experimental data.

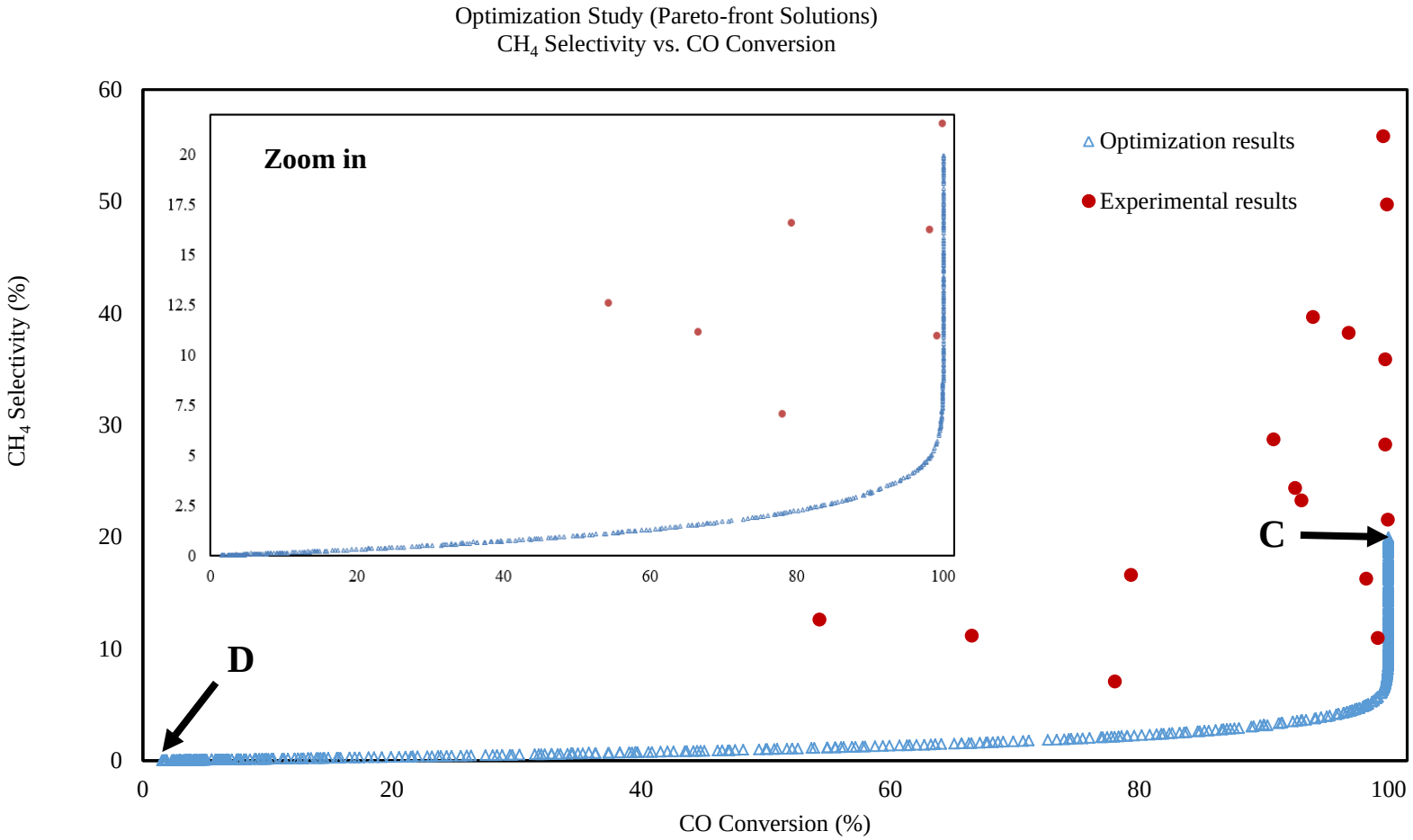

Figure 20 Pareto-front solutions obtained by optimization (between CH_4 selectivity and CO conversion) and its comparison with experimental data.

The boundary conditions of the process parameters considered for the optimization procedure are listed in Table 9. The best two experimental data in terms of selectivities of CH_4, CO_2 and C_{5+} products as well as CO conversion were selected for comparison with the optimization results. The pie charts (Figure 21 to Figure 23) show the results of selectivities at the selected runs as well as that obtained from the optimization procedure. Also, the values of CO conversion and CO_2 selectivity, together with the process operating conditions, were given in the chart for comparison. It can be seen that better outcomes were obtained from the optimization study for all the objectives compared to those of the experiments. In detail, the optimization study showed the optimum CO conversion at 94.26%, which is better than that of Exp. 01 at 78.04% but not as good as Exp. 06 (see Table 4 and 5 in the previous study [14]) at 99.15%. However, with regard to C_{5+} and CH_4 selectivities, the optimization case indicated the optimum selectivities were at 91.06% and 6.57%, respectively while C_{5+} selectivity was obtained at 90.45% and 85.30% for Exp. 01 and Exp. 06 (see Table 4 and 5 in the previous study [14]), and CH_4 selectivity was about 7.06% and 10.96%, respectively. Hence, the performance of the FTS was improved with respect to the desired C_{5+} and undesired CH_4 selectivity. Last but not least, CO_2 selectivity determined from the optimization procedure was almost zero, while that of the optimum experiential runs measured CO_2 values at 4.52% and 14.68%. The optimum selected condition from the optimization data-set was achieved at T = 485 *K*, P = 30 *bar*, GHSV = 1800 $Nm\ell\ (STP)\ g_{cat}^{-1}\ h^{-1}$ and H_2/CO = 2.6. It is apparent that better global output was attained at low temperature, space velocity, high pressure and inlet hydrogen-to-carbon monoxide molar ratio.

Table 9 Boundary conditions considered for optimization with respect to reaction temperature, total pressure and space velocity and carbon monoxide molar ratio

Temperature range (*K*)	Pressure range (*bar*)	Space velocity range ($Nm\ell\ (STP)\ g_{cat}^{-1}\ h^{-1}$)	H_2/CO range (*mol/mol*)
470-530	1-30	1800-6000	1-3.2

The trends herein reported, manifest that a compromise has to be found in the selection of the process conditions in order to find the optimal operating set-point. The developed model and overall kinetics mechanism reported, together with the optimization procedure presented herein, represented a key tool for such an investigation.

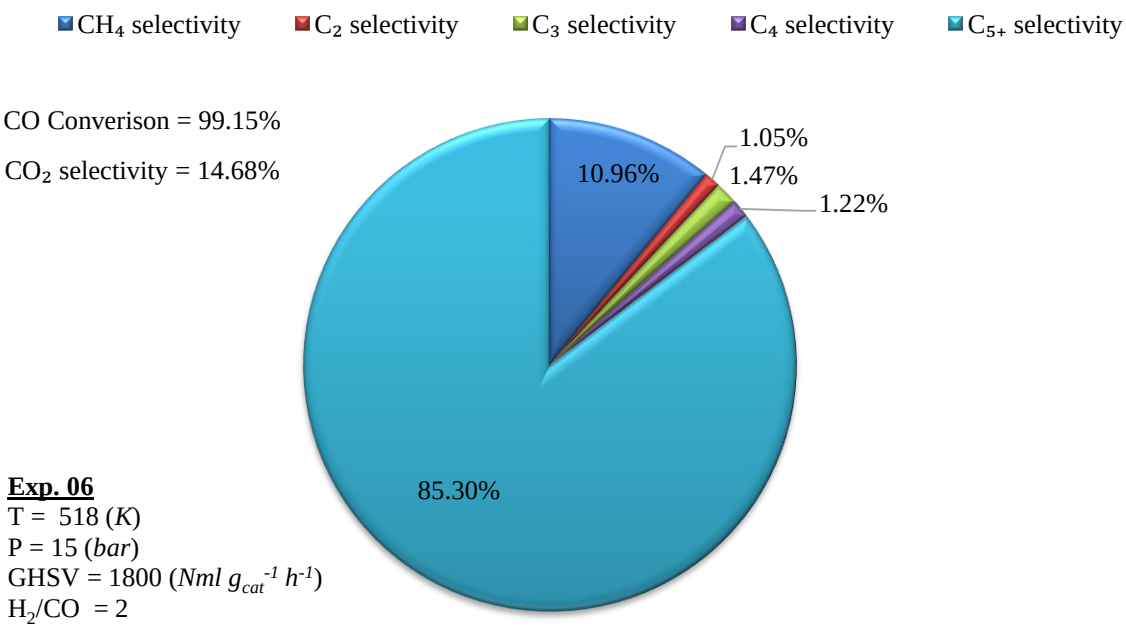

Figure 21 The first optimum experimental results.

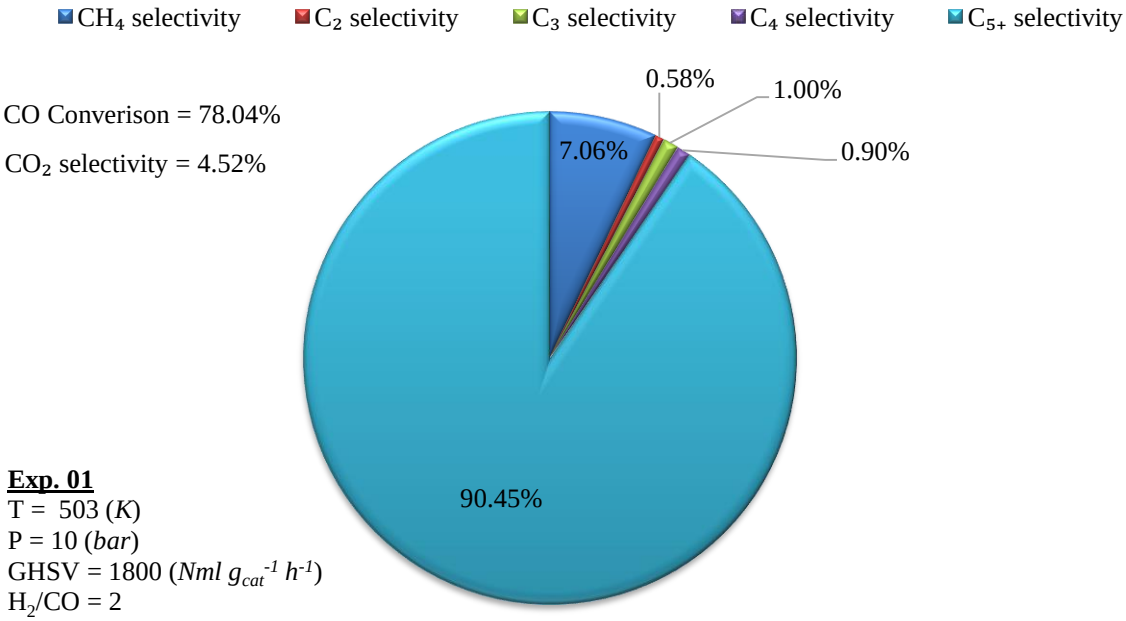

Figure 22 The second optimum experimental results.

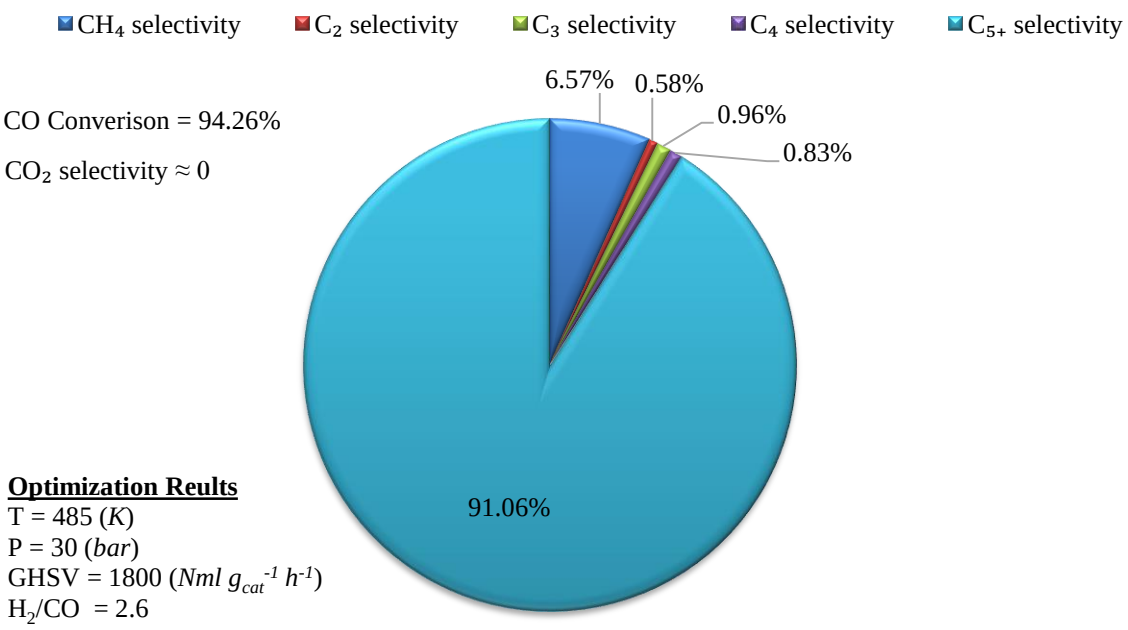

Figure 23 The optimum results obtained from multi-objective optimization (using NSGA–II).

4. Conclusion

The capability of the developed mathematical model for calculating the trend of changes of reactant and products' concentrations, partial pressures, mole fractions as well as conversion and selectivities was highlighted. Such outcomes are profoundly beneficial in reactor design, scale-up, the understanding of its behaviour in operation and predicting the effect of changing operating conditions which highlights the effectiveness of the develop mathematical tool. The developed mathematical model was employed to conduct parametric studies (sensitivity analysis) as well as multi-objective optimization of FTS global performance parameters using NSGA-II. Initially, the parametric studies were conducted to identify those input variables that have the most significant effect on conversion and selectivity of products species.

The results indicated that the increase of reaction temperature had positive influence on catalytic activity and its performance in terms of conversion of syngas compositions. However, increasing the temperature had also an adverse impact as it resulted in increased CO_2 selectivity and the shift toward low molecular weight hydrocarbons products (i.e. Methane, olefins: C_2-C_3, paraffins: C_2-C_7) over the Co/SiO_2 catalyst. In contrast, it was shown that the formation of heavier hydrocarbons (C_{5+}) was favoured at low temperatures. All the reaction rates were enhanced upon increasing temperature ($R_j \propto T$), hence more reactants were consumed and more products were formed. However, the results manifested that the products distributions were not directly proportional to the temperature (in the case of higher molecular weight) as it is explained by the nature of the chain growth probability (α) defined by the rate of propagation (growth) and termination steps. It was shown that α was inversely proportional to termination reaction rate ($\alpha \propto 1/R_t$). Meanwhile, the mole and mass fraction of heavier hydrocarbons increased upon increasing the α value. This justified why the increase of temperature led

to lower liquid product selectivity, while the higher light hydrocarbons formed. Moreover, methane had higher temperature dependency compared to other hydrocarbons due to its lower activation barriers and hence its production rate increased faster than other light hydrocarbons.

The highest CO and H_2 conversions were obtained at the lowest GHSV values. This was true as a low GHSV is associated with a high residence time so that the reactants have sufficient time to react and subsequently their concentrations decrease. The results indicated that the selectivities of heavy FT products were sensitive to space velocity changes on Co/SiO_2 catalyst, while this parameter was the key element to attain the high conversion rates (of CO and H_2). GHSV, similarly to the temperature factor, had substantial impact on the catalytic activity, reaction kinetics and overall performance of the reactor. It was shown that the CO and H_2 consumptions are more sensitive to GHSV at lower temperature condition. In addition, the results manifested the substantial increase of selectivity of heavy products and the decrease of that of methane upon increasing the space velocity, suggesting that the increase of space velocity leads to the elimination of mass transfer resistance so that the dominant effects of diffusional limitation yield the removal of hydrocarbons from the active sites at the surface of the catalyst. Therefore, the increase of GHSV favours the production of long chain heavy hydrocarbon components, while CH_4 selectivity, as expected, goes in the opposite direction.

Pressure effects were also considerable in that the increase in total pressure moved the product selectivities towards heavy products due to hydrocarbons condensation, which are normally in the gaseous state at atmospheric pressure. In fact, the saturation of catalyst pores by liquid formation happens at high pressure condition. The changes of CO and H_2 conversions were proportional to the total pressure: increasing pressure resulted in the increment of CO and H_2 conversions. Also, the selectivity C_2-C_7 paraffins decreased upon increase of the total pressure. Such variation manifested the faster reduction of the hydrocarbon compounds with lower carbon atom number. Hence, the increase of the total pressure had adverse effect on tail gas and LPG productions which exhibited the increase of pressure condition is not desirable if the low chain hydrocarbons are preferable products. Similar behaviours were observed for light olefin components; whereas the olefins to paraffins ratio were not changed. CH_4 selectivity decrease substantially with the increasing of the pressure, which is a favourable condition as this component is undesired FT products. The CO and H_2 conversion increased faster at lower total pressure (e.g. 1-10 *bar*) compared to that of the higher range of 10-20 *bar*; suggesting that the syngas consumption rate is more sensitive to total pressure at its lower range.

The increase of H_2/CO ratio in the inlet reactants led to different proportion of adsorbed hydrogen and surface carbon atoms. CO and H_2 had respectively inhibiting and positive impacts on the rate of reaction, suggesting that the CO consumption rate increases with rising the H_2/CO ratio whereas that of H_2 decreases upon the increase of the molar ratio. This also resulted in enhancing hydrogen concentration on the active sites and increasing the hydrogenation degree of highly concentrated monomers and accelerating the rate of chain termination step. This caused faster desorption of products rather than incorporating to the chain growth, which resulted in a substantial reduction of selectivity of heavy FT products and a subsequent increase of light hydrocarbons (C_2-C_7). Also, the results manifested that the major loss of liquid (C_{5+}) formation was due to methanation reaction in which the C_{5+} and methane selectivities changed from about 93% to 72% and 5% to 20% respectively with increasing the H_2/CO ratio from 1 to 3.5 (*mol/mol*). The olefins/paraffins ratio slightly decreased upon the increasing of the

H_2/CO molar ratio, while the CO_2 selectivity decreased from about 15% to 1%; which implied the slight water gas shift activity at low H_2/CO ratio. It was found from the kinetic model and governed equations that the water gas shift reaction rate is inversely proportional to the H_2/CO ratio and one can conclude that the partial pressures of both reactants as well as their proportion have substantial effects on the rate of CO_2 formation. In addition, the trend of changes of R_{WGS} (water gas shift reaction rate) along the axial dimension of the tube length at different H_2/CO molar ratio was illustrated in which the rate decreased from 1.4964×10^{-5} to 1.987×10^{-7} $mol\ g_{cat}^{-1}\ s^{-1}$ upon the increasing of the molar ratio from 1 to 3.5 *mol/mol*.

The results indicated that reaction temperature, total pressure, space velocity and H_2/CO molar ratio had all substantial influence on the performances. Hence, all parameters were considered in the multi-objective optimization process using Non-Dominated Sorting Genetic Algorithm (NSGA–II) to optimize the fitness functions (i.e. objective functions). Due to the conflicting objective functions, single values of the input variables could not satisfy all the objective functions simultaneously. For instance, any operating conditions that increased the CO conversion, reduced C_{5+} selectivity while increased the undesirable CH_4 selectivity. Thus, the optimum solution was presented in the form of Pareto-fronts in which each individual points on these lines presented an optimum solution. The trends of Pareto-fronts were so that the selection of input variables for optimum performance required a compromise between different objectives. Such results serve as an optimal database that can be considerably helpful for the selection of the optimal operating conditions for maximum performance of FT process depending on the priority of the objective functions. The optimization results showed that the optimum C_{5+} and CH_4 selectivities were at 91.06% and 6.57%, respectively and the CO_2 selectivity determined from the optimization procedure was almost zero whereas the CO conversion was 94.26%. The optimum selected condition from the optimization data-set was achieved at T = 485 *K*, P = 30 *bar*, GHSV = 1800 Nmℓ (STP) g_{cat}^{-1} h^{-1} and H_2/CO = 2.6. It is apparent that better global output was attained at low temperature, space velocity, high pressure and inlet hydrogen-to-carbon monoxide molar ratio.

5. Acknowledgement

The main author (Nima Moazami) would like to extend thanks to the provision of a Ph.D. scholarship to the Department of Mechanical Engineering, The University of Birmingham, UK. This opportunity enabled him to continue the work on the modelling of fuel reforming and FTS reactors.

Supporting Information.

6. References

1. Mahmoudi, H. Performance of cobalt-based eggshell catalyst in low temperature Fischer-Tropsch synthesis process to produce long-chain hydrocarbons from synthesis gas utilizing fixed-bed reactor technology. University of Birmingham, 2015.
2. Wang, Y.-N.; Li, Y.-W.; Bai, L.; Zhao, Y.-L.; Zhang, B.-J., Correlation for gas–liquid equilibrium prediction in Fischer–Tropsch synthesis. *Fuel* **1999,** *78* (8), 911-917.
3. Fu, T.; Jiang, Y.; Lv, J.; Li, Z., Effect of carbon support on Fischer–Tropsch synthesis activity and product distribution over Co-based catalysts. *Fuel Processing Technology* **2013,** *110*, 141-149.
4. Gill, S.; Tsolakis, A.; Dearn, K.; Rodríguez-Fernández, J., Combustion characteristics and emissions of Fischer–Tropsch diesel fuels in IC engines. *Progress in Energy and Combustion Science* **2011,** *37* (4), 503-523.
5. Hadnađev-Kostić, M. S.; Vulić, T. J.; Marinković-Nedučin, R. P.; Nikolić, A. D.; Jović, B., Mg-Fe-mixed oxides derived from layered double hydroxides: a study of the surface properties. *Journal of the Serbian Chemical Society* **2011,** *76* (12), 1661-1671.
6. Lira, E.; López, C. M.; Oropeza, F.; Bartolini, M.; Alvarez, J.; Goldwasser, M.; Linares, F. L.; Lamonier, J.-F.; Pérez Zurita, M. J., HMS mesoporous silica as cobalt support for the Fischer–Tropsch Synthesis: Pretreatment, cobalt loading and particle size effects. *Journal of Molecular Catalysis A: Chemical* **2008,** *281* (1–2), 146-153.
7. Kim, C.-U.; Kim, Y.-S.; Chae, H.-J.; Jeong, K.-E.; Jeong, S.-Y.; Jun, K.-W.; Lee, K.-Y., Effect of cobalt catalyst type and reaction medium on Fischer-Tropsch synthesis. *Korean J. Chem. Eng.* **2010,** *27* (3), 777-784.
8. Yang, J. H.; Kim, H.-J.; Chun, D. H.; Lee, H.-T.; Hong, J.-C.; Jung, H.; Yang, J.-I., Mass transfer limitations on fixed-bed reactor for Fischer–Tropsch synthesis. *Fuel Processing Technology* **2010,** *91* (3), 285-289.
9. Moazami, N.; Wyszynski, M. L.; Mahmoudi, H.; Tsolakis, A.; Zou, Z.; Panahifar, P.; Rahbar, K., Modelling of a fixed bed reactor for Fischer–Tropsch synthesis of simulated N_2-rich syngas over Co/SiO_2: Hydrocarbon production. *Fuel* **2015,** *154* (0), 140-151.
10. Pour, A. N.; Zamani, Y.; Tavasoli, A.; Kamali Shahri, S. M.; Taheri, S. A., Study on products distribution of iron and iron–zeolite catalysts in Fischer–Tropsch synthesis. *Fuel* **2008,** *87* (10), 2004-2012.
11. Atashi, H.; Mansouri, M.; Hosseini, S.; Khorram, M.; Mirzaei, A.; Karimi, M.; Mansouri, G., Intrinsic kinetics of the Fischer-Tropsch synthesis over an impregnated cobalt-potassium catalyst. *Korean J. Chem. Eng.* **2012,** *29* (3), 304-309.
12. Moazami, N.; Mahmoudi, H.; Panahifar, P.; Rahbar, K.; Tsolakis, A.; Wyszynski, M. L., Mathematical Modeling and Performance Study of Fischer-tropsch Synthesis of Liquid Fuel over Cobalt-silica. *Energy Procedia* **8/2015,** *75*, 62-71.
13. Borg, Ø.; Dietzel, P. D. C.; Spjelkavik, A. I.; Tveten, E. Z.; Walmsley, J. C.; Diplas, S.; Eri, S.; Holmen, A.; Rytter, E., Fischer–Tropsch synthesis: Cobalt particle size and support effects on intrinsic activity and product distribution. *Journal of Catalysis* **2008,** *259* (2), 161-164.
14. Moazami, N.; Wyszynski, M. L.; Rahbar, K.; Tsolakis, A.; Mahmoudi, H., A comprehensive study of kinetics mechanism of Fischer-Tropsch synthesis over cobalt-based catalyst. *Chemical Engineering Science* **2017,** *171*, 32-60.
15. Moazami, N.; Mahmoudi, H.; Rahbar, K.; Panahifar, P.; Tsolakis, A.; Wyszynski, M. L., Catalytic performance of cobalt–silica catalyst for Fischer–Tropsch synthesis: Effects of reaction rates on efficiency of liquid synthesis. *Chemical Engineering Science* **2015,** *134*, 374-384.
16. Atwood, H. E.; Bennett, C. O., Kinetics of the Fischer-Tropsch reaction over iron. *Industrial & Engineering Chemistry Process Design and Development* **1979,** *18* (1), 163-170.
17. Bub, G.; Baerns, M.; Büssemeier, B.; Frohning, C., Prediction of the performance of catalytic fixed bed reactors for Fischer-Tropsch synthesis. *Chemical Engineering Science* **1980,** *35* (1), 348-355.
18. De Swart, J. W. A.; Krishna, R.; Sie, S. T., Selection, design and scale up of the Fischer-Tropsch reactor *Studies in Surface Science and Catalysis* **1997,** *107*, 213-218.
19. Jess, A.; Popp, R.; Hedden, K., Fischer–Tropsch synthesis with nitrogen-rich syngas: fundamentals and reactor design aspects. *Applied Catalysis A: General* **1999,** *186* (1), 321-342.
20. Wang, Y.-N.; Ma, W.-P.; Lu, Y.-J.; Yang, J.; Xu, Y.-Y.; Xiang, H.-W.; Li, Y.-W.; Zhao, Y.-L.; Zhang, B.-J., Kinetics modelling of Fischer–Tropsch synthesis over an industrial Fe–Cu–K catalyst. *Fuel* **2003,** *82* (2), 195-213.
21. Guettel, R.; Turek, T., Comparison of different reactor types for low temperature Fischer–Tropsch synthesis: A simulation study. *Chemical Engineering Science* **2009,** *64* (5), 955-964.
22. Jess, A.; Kern, C., Modeling of Multi-Tubular Reactors for Fischer-Tropsch Synthesis. *Chemical engineering & technology* **2009,** *32* (8), 1164-1175.

23. Philippe, R.; Lacroix, M.; Dreibine, L.; Pham-Huu, C.; Edouard, D.; Savin, S.; Luck, F.; Schweich, D., Effect of structure and thermal properties of a Fischer–Tropsch catalyst in a fixed bed. *Catalysis Today* **2009,** *147*, S305-S312.
24. Rafiq, M. H.; Jakobsen, H. A.; Schmid, R.; Hustad, J. E., Experimental studies and modeling of a fixed bed reactor for Fischer–Tropsch synthesis using biosyngas. *Fuel processing technology* **2011,** *92* (5), 893-907.
25. Park, N.; Kim, J.-R.; Yoo, Y.; Lee, J.; Park, M.-J., Modeling of a pilot-scale fixed-bed reactor for iron-based Fischer–Tropsch synthesis: Two-dimensional approach for optimal tube diameter. *Fuel* **2014,** *122* (0), 229-235.
26. de Klerk, A.; Furimsky, E., *Catalysis in the refining of Fischer-Tropsch Syncrude*. Royal Society of Chemistry: 2010.
27. Satterfield, C. N.; Huff Jr, G. A.; Stenger, H. G.; Carter, J. L.; Madon, R. J., A comparison of Fischer-Tropsch synthesis in a fixed-bed reactor and in a slurry reactor. *Industrial & engineering chemistry fundamentals* **1985,** *24* (4), 450-454.
28. Leckel, D., Diesel production from Fischer−Tropsch: the past, the present, and new concepts. *Energy & Fuels* **2009,** *23* (5), 2342-2358.
29. Dry, M. E., Practical and theoretical aspects of the catalytic Fischer-Tropsch process. *Applied Catalysis A: General* **1996,** *138* (2), 319-344.
30. Dry, M., The Fischer-Tropsch Synthesis. *Catalysis science and technology* **1981,** *1*, 159-255.
31. Dry, M. E., The Fischer–Tropsch process: 1950–2000. *Catalysis today* **2002,** *71* (3), 227-241.
32. Jager, B.; Espinoza, R., Advances in low temperature Fischer-Tropsch synthesis. *Catalysis Today* **1995,** *23* (1), 17-28.
33. Bukur, D. B.; Lang, X.; Akgerman, A.; Feng, Z., Effect of Process Conditions on Olefin Selectivity during Conventional and Supercritical Fischer−Tropsch Synthesis. *Industrial & Engineering Chemistry Research* **1997,** *36* (7), 2580-2587.
34. Bai, L.; Hong-Wei, X.; Yong-Wang, L.; Yi-Zhuo, H.; Bing, Z., Slurry phase Fischer–Tropsch synthesis over manganese-promoted iron ultrafine particle catalyst. *Fuel* **2002,** *81* (11-12), 1577-1581.
35. Khodakov, A. Y.; Griboval-Constant, A.; Bechara, R.; Zholobenko, V. L., Pore Size Effects in Fischer Tropsch Synthesis over Cobalt-Supported Mesoporous Silicas. *Journal of Catalysis* **2002,** *206* (2), 230-241.
36. Visconti, C. G.; Tronconi, E.; Lietti, L.; Forzatti, P.; Rossini, S.; Zennaro, R., Detailed kinetics of the Fischer–Tropsch synthesis on cobalt catalysts based on H-assisted CO activation. *Topics in Catalysis* **2011,** *54* (13-15), 786-800.
37. Yang, J.; Liu, Y.; Chang, J.; Wang, Y.-N.; Bai, L.; Xu, Y.-Y.; Xiang, H.-W.; Li, Y.-W.; Zhong, B., Detailed kinetics of Fischer-Tropsch synthesis on an industrial Fe-Mn catalyst. *Industrial & engineering chemistry research* **2003,** *42* (21), 5066-5090.
38. van Herk, D.; Castaño, P.; Quaglia, M.; Kreutzer, M. T.; Makkee, M.; Moulijn, J. A., Avoiding segregation during the loading of a catalyst–inert powder mixture in a packed micro-bed. *Applied Catalysis A: General* **2009,** *365* (1), 110-121.
39. Froment, G. F.; Bischoff, K. B.; De Wilde, J., *Chemical reactor analysis and design*. Wiley New York: 1990; Vol. 2.
40. Song, D.; Li, J., Effect of catalyst pore size on the catalytic performance of silica supported cobalt Fischer–Tropsch catalysts. *Journal of Molecular Catalysis A: Chemical* **2006,** *247* (1), 206-212.
41. Deb, K., *Multi-Objective Optimization using Evolutionary Algorithms*. John Wiley & sons Ltd: 2001.
42. Gen, M.; Cheng, R., *Genetic Algorithms and Engineering Optimizations*. 1st ed ed.; John Wiley and sons: Canada, 2000.
43. Goldberg, D. E., *Genetic Algorithms in Search, Optimization and Machine Learning*. Addison-Wesley Longman Publishing Co., Inc.: 1989; p 372.
44. Konak, A.; Coit, D. W.; Smith, A. E., Multi-objective optimization using genetic algorithms: A tutorial. *Reliability Engineering & System Safety* **2006,** *91* (9), 992-1007.
45. Guide, G. O. T. U. s., The MathWorks, Inc. Version 3.2.4 ed.; R2013b, Ed. 2013.

Abstract Graphic